Tectonics

RESEARCH ARTICLE
10.1029/2021TC006913

Key Points:

- Pre- and syn-orogenic structural inheritance controlled first-order fold geometry
- Pre-folding structural fabrics determined fold kinematics and syn-folding deformation pattern
- The deformation pattern exposed in the anticline significantly differs from classical folding-related templates

Correspondence to:
L. R. Berio,
luigi.berio@gmail.com

Citation:
Berio, L. R., Storti, F., Balsamo, F., Mittempergher, S., Bistacchi, A., & Meda, M. (2021). Structural evolution of the Parmelan anticline (Bornes Massif, France): Recording the role of structural inheritance and stress field changes on the finite deformation pattern. *Tectonics*, *40*, e2021TC006913. https://doi.org/10.1029/2021TC006913

Received 21 MAY 2021
Accepted 12 OCT 2021

Author Contributions:
Conceptualization: L. R. Berio, F. Storti, F. Balsamo, S. Mittempergher, A. Bistacchi, M. Meda
Data curation: L. R. Berio
Funding acquisition: F. Storti, A. Bistacchi
Investigation: L. R. Berio, F. Storti, F. Balsamo, S. Mittempergher, A. Bistacchi, M. Meda
Methodology: L. R. Berio, F. Storti, F. Balsamo, S. Mittempergher, A. Bistacchi, M. Meda
Project Administration: M. Meda
Writing – original draft: L. R. Berio, F. Storti
Writing – review & editing: F. Balsamo, S. Mittempergher, A. Bistacchi

Structural Evolution of the Parmelan Anticline (Bornes Massif, France): Recording the Role of Structural Inheritance and Stress Field Changes on the Finite Deformation Pattern

L. R. Berio[1], F. Storti[1], F. Balsamo[1], S. Mittempergher[2], A. Bistacchi[3], and M. Meda[4]

[1]Università degli Studi di Parma, Dipartimento di Scienze Chimiche, della Vita e della Sostenibilità Ambientale, NEXT - Natural and Experimental Tectonics Research Group, Parma, Italy, [2]Dipartimento di Scienze Chimiche e Geologiche, Università degli Studi di Modena e Reggio Emilia, Modena, Italy, [3]Dipartimento di Scienze dell'Ambiente e della Terra, Università degli Studi di Milano Bicocca, Milano, Italy, [4]Eni Spa, Upstream and Technical Services, San Donato Milanese, Italy

Abstract In many orogenic wedges, foreland basin systems are preferential sites for economical resource accumulation, typically hydrocarbons. Understanding how structural inheritance perturbs the evolution of folding-related deformation and impacts on subsurface fracture patterns bears first order economic and environmental implications, when also CO_2 storage is considered. Studying properly selected field analogs of buried anticlines provides fundamental information on fracture patterns at the subseismic scale. The Parmelan anticline is a flat-topped box-fold located in the Bornes Massif (France) involving Lower Cretaceous platform carbonates (Urgonian Limestones). We studied this field analogue by combining structural analysis with syntectonic calcite vein petrography and geochemistry to unravel the progression of deformation and to obtain constraints on the regional stress field evolution. We documented (a) a network of pre-folding hinge-parallel and hinge-perpendicular extensional fault zones, (b) two deformation assemblages developed during pre-folding layer-parallel-shortening under different stress configurations including veins, bed-perpendicular stylolites and subsidiary reverse faults, (c) a limited occurrence of localized syn-folding deformation structures (i.e., hinge-parallel veins), and (d) an association of veins and stylolites oblique to the fold axial trend, formed in a post-folding stage. We propose that pre- and syn-orogenic inherited structures controlled first-order fold geometry and partial development of classical syn-folding deformation features. Moreover, our data reveal a complex stress history marked by permutations of the vertical principal stress axis from strike-slip to purely compressional stress regimes and vice versa, accompanied by a progressive counterclockwise rotation of the horizontal maximum stress axis.

1. Introduction

Deformation patterns in shallow crustal sectors exhumed at mountain fronts typically record evolutionary pathways that mostly occurred in the subsurface of foreland basin systems, where deformation and sedimentation commonly interact (DeCelles & Giles, 1996). Thrust-related fold growth is controlled by two major factor categories (e.g., Tavani, Storti et al., 2015), namely: (a) stress field and environmental conditions of deformation; (b) mechanical stratigraphy and structural inheritance of deformed multilayers.

Regional stress fields driving deformation in foreland basin systems are influenced by both internal and external factors. The former include: (a) the local tectonic regime, with typically extensional regimes in the back-bulges, forebulges and outer foredeeps, replaced by contractional regimes in inner foredeeps and thrust wedge toes; (b) the thickness of syn-orogenic sediments in foredeeps; (c) the along strike pattern of uplift and subsidence in forebulges and foredeeps, respectively (e.g., Tavani, Storti et al., 2015). External factors, which typically derive from tectonic plate interactions at convergent margins, include the occurrence of rigid indenters and block rotations about vertical axes, and variations through time in convergence directions and rates (e.g., Branellec et al., 2015; Homberg et al., 1999; Lickorish et al., 2002; Philippe et al., 1998; Platt et al., 1989).

Long tectonic journeys of former foreland regions, from initial subsidence in back-bulge basins to incorporation within thrust wedges, may involve stress field changes, either of principal axis trajectories or intensities, or both (e.g., Amrouch et al., 2011; Beaudoin et al., 2012; Evans et al., 2012; Ferrill et al., 2021; Tavani, Storti, et al., 2011; Tavani, Storti et al., 2015; Vitale et al., 2012). Stress field rotations and permutations are an important factor that influences finite deformation patterns in folds (e.g., Beaudoin et al., 2012, 2016). Field studies are essentials for constraining the evolution of regional stress fields through space and time, thus improving our knowledge on the evolution of orogenic systems (e.g., Beaudoin et al., 2016; Muñoz et al., 2013; Quintà & Tavani, 2012; Tavani, Mencos, et al., 2011), including the complex interplay between contraction and extension during thrust sheet stacking in foredeeps and thrust wedge toes, with relevant implications for the geological hazard component of seismic risk in foreland basin systems (e.g., Storti et al., 2018).

In foreland basin systems, pre-orogenic fault zones can provide preferential structural weaknesses that strongly influence stress concentration and coseismic failure during orogenic contraction (e.g., Carannante et al., 2015). Furthermore, the early stages of syn-orogenic deformation in forebulges and foredeeps typically produce incremental structural heterogeneity and anisotropy that influence further progression of fracturing and folding within thrust wedges (e.g., Tavani, Storti et al., 2015). Contractional overprinting of both pre- and syn-orogenic structural inheritance developed ahead of orogens can provide effective pathways to accommodate layer parallel shortening, commonly by buttressing against inherited extensional fault zones and their positive inversion (e.g., Butler, 1989; Letouzey, 1990; Scisciani, 2009; Scisciani et al., 2001; Welbon, 1988), producing deformation patterns that significantly differ from predictive templates obtained by mechanical and kinematical modeling of faulting and folding in undeformed layer-cake stratigraphy (e.g., Erickson & Jamison, 1995; Lemiszki et al., 1994; Salvini & Storti, 2001; Storti & Salvini, 1996; Tavani, Storti, et al., 2011). Furthermore, exploiting pre-existing mechanical weakness zones, even when partly misoriented, can prevent widespread development of folding-related longitudinal (hinge parallel) and transversal (at high angle to fold hinge) deformation structures (e.g., Bellahsen et al., 2006; Bergbauer & Pollard, 2004; Vitale et al., 2012).

A deep understanding of the incremental development of natural deformation patterns through detailed studies of field analogs, including those involving structural inheritance, provides robust constraints to predictive structural modeling of fracture distributions in folds buried in foreland basin systems and associated fluid flow in hydrocarbon reservoirs and aquifers (e.g., Butler, 1991; Ferket et al., 2003; Gutmanis et al., 2018; Hennings et al., 2000; Roure et al., 2005; Stephenson et al., 2007; Van Geet et al., 2002; Vilasi et al., 2009). Despite the mechanical impact of inherited pre-folding fabrics to influence development of folding-related deformation patterns has been explored using geomechanical modeling and natural case studies (e.g., Guiton, Leroy, et al., 2003; Guiton, Sassi, et al., 2003; Sassi et al., 2012), further work for learning from nature is still necessary.

In this contribution, we report on the structural evolution of the Parmelan anticline, in the Bornes Massif of the external French Alps (Figure 1). The anticline involves a pre-folding extensional fault system trending parallel to the fold axis and is characterized by a spectacularly exposed flat-lying crestal plateau that facilitates detailed geologic studies (Figure 2). By combining structural field data with calcite-filled vein petrography and geochemistry, we unraveled the progressive evolution of the deformation pattern and documented the role of structural inheritance to constrain fold kinematics and produce a peculiar folding-related deformation pattern, quite different from those associated with parallel folding of layer-cake stratigraphy (e.g., Tavani et al., 2006, 2008). The structural pattern exposed in the Parmelan anticline supports the occurrence of rotations and permutations of the regional principal stresses, in the framework of the progressive incorporation of a foreland basin sector into the Alpine orogenic wedge.

2. Geological Outline

The Alps originated by subduction and closure of the Piedmont-Ligurian ocean and by the collision between the European and Adriatic continental margins since Cretaceous times (Dal Piaz et al., 2003 and references therein). In this geodynamic framework, the Helvetic-Dauphinois domain formed by the shortening of the proximal European margin (e.g., de Graciansky et al., 1989; Lemoine et al., 1986). The Bornes Massif

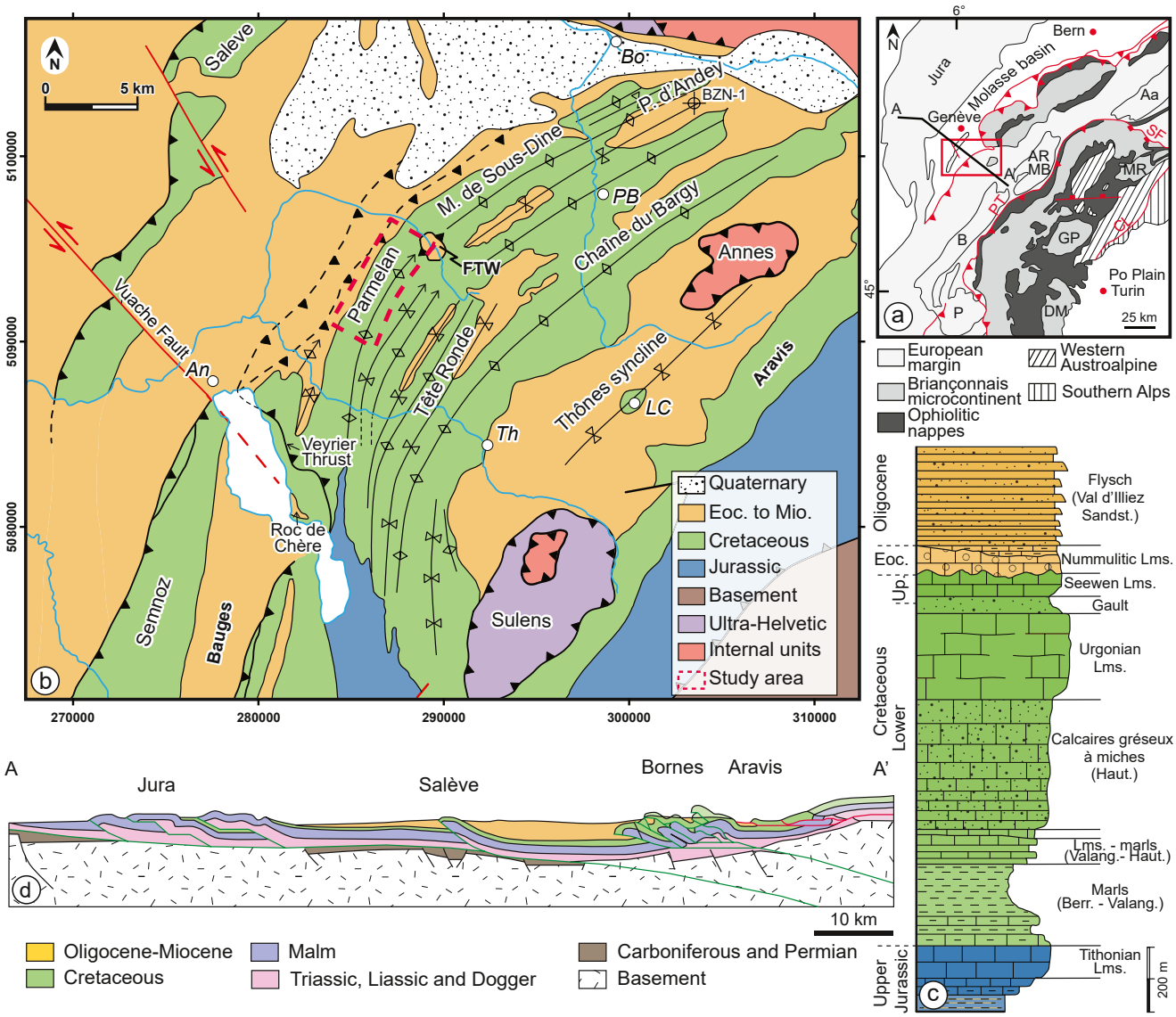

Figure 1. (a) Simplified tectonic map of the western Alps (modified after Egli & Mancktelow, 2013) with the location of the study area. External Crystalline massifs: P, Pelvoux; B, Belledonne; AR, Aiguilles Rouge; MB, Mont Blanc; Aa, Aar. Internal Crystalline massifs: DM, Dora Maira; GP, Gran Paradiso; MR, Monte Rosa. PT, Penninic thrust; CL, Canavese line; SF, Simplon fault. (b) Geological-structural sketch map of the Bornes Massif region (modified after Butler, 1992; Charollais et al., 1988; Deville & Sassi, 2006; Deville et al., 1994; Doudoux et al., 1992; Gidon, 1996; Guellec et al., 1990; Huggenberger & Wildi, 1991). An, Annecy; Th, Thônes; LC, La Clusaz; PB, Le Petit-Bornand-les-Glières; Bo, Bonneville. FTW: Fillière Tectonic Window. BZN-1, Brizon well from Charollais & Jamet, 1990. (c) Schematic stratigraphic column of the Mesozoic and Tertiary succession exposed in the Bornes Massif (modified after Charollais et al., 1977, 1988). (d) Balanced cross-section through the Jura-Bornes Massif (redrawn from Bellahsen et al., 2014).

belongs to the northern Subalpine chains of the Dauphinois domain of SE France and is located between the Savoy Molasse Basin to the NW (i.e., plateau molassique sensu Charollais et al., 1988) and the External Crystalline Massifs to the SE (Figure 1a; e.g., Bellahsen et al., 2014). The Bornes Massif provides spectacular exposures of folded Mesozoic European passive margin succession and the overlying Cenozoic foreland basin system sediments (Figure 1c; e.g., Charollais et al., 1988; Huggenberger & Wildi, 1991). The Mesozoic succession is mainly composed of limestones and shales (e.g., Charollais et al., 1988; Moss, 1992). In particular, the Lower Cretaceous stratigraphy is dominated by the 200 m-thick Late Hauterivian-Early Aptian platform carbonates (Urgonian Limestones) and by the underlying 400 m-thick Hauterivian siliceous limestones (Calcaires gréseux à miches; e.g., Charollais et al., 1988; Clavel et al., 2013). These formations are overlain by Aptian-Cenomanian glauconitic sandstones (Gault, "Formation des grès verts des Aravis") and

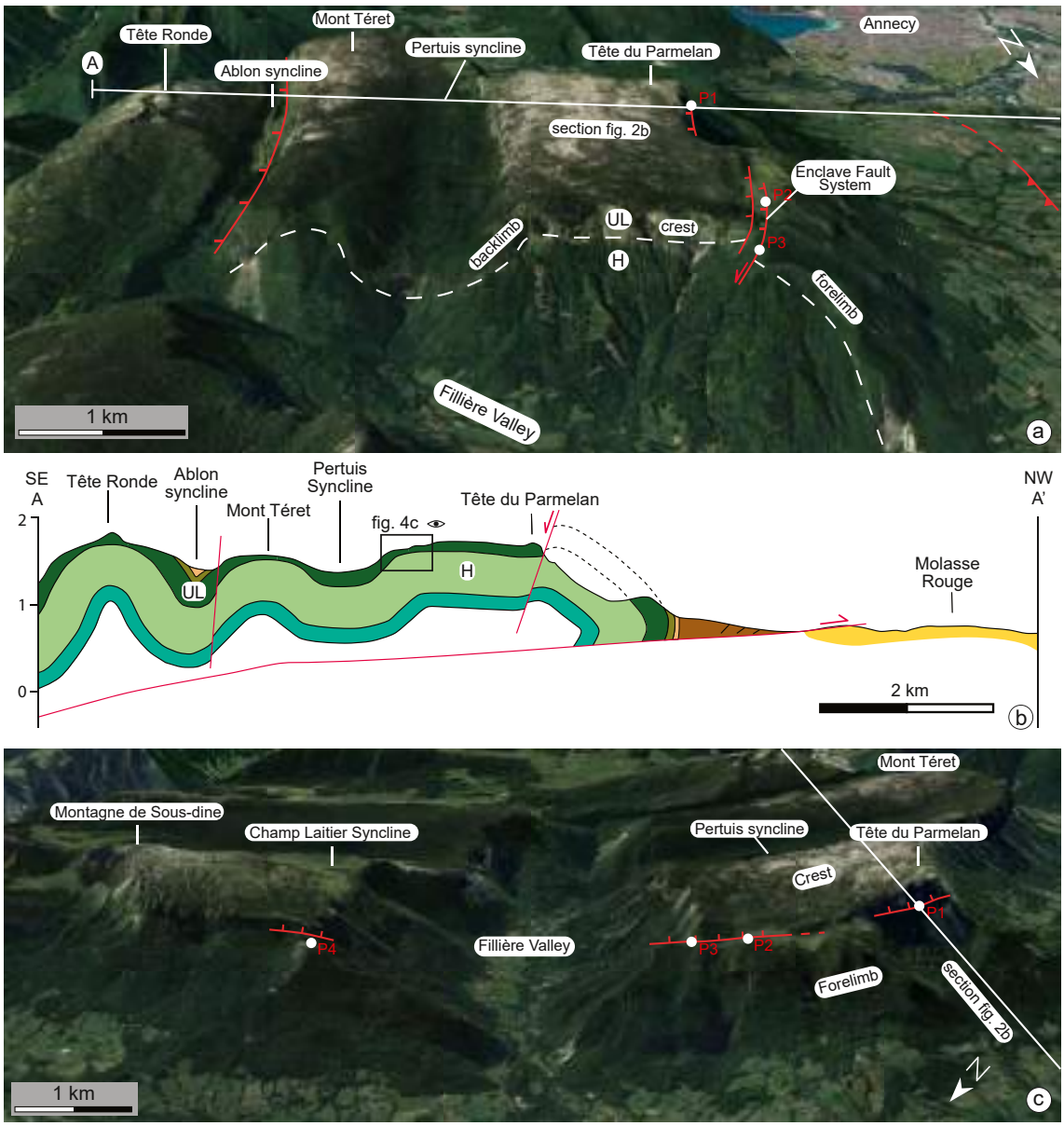

Figure 2. (a) Cross-sectional panoramic view (Google Earth image), looking toward SW, of the Fillière Valley transect showing the Tête Ronde, Mont Téret and Parmelan anticlines and the longitudinal extensional fault systems (LF). UL, Urgonian Limestones; H, Hauterivian Calcaires gréseux à miches. The white dashed line represents the Urgonian Limestones- Calcaires gréseux à miches limit. P1-P3 are structural sites (see text for details). (b) NW-SE geologic cross-section through the Tête Ronde, Mont Téret and Parmelan anticlines. Section trace in Figures 2a, 2c, and 3a. UL, Urgonian Limestones; H, Hauterivian Calcaires gréseux à miches. (c) Panoramic view (Google Earth image), looking toward SE, of the Montagne de Sous-Dine–Parmelan anticline with the position of the Enclave Fault System (LF) at the crest-forelimb transition. P1–P4 are structural sites.

by the Turonian-Santonian "sublithographic limestones" (Calcaires de Seewen; Charollais et al., 1988). A major regional unconformity marks the transition from Cretaceous to Eocene limestones and marls and the overlying Oligocene flysch ("Val d'Illiez Sandstones" in the external Bornes; Figure 1c; Lateltin, 1988; Menkveld-Gfeller et al., 2016; Sayer, 1995). In the Savoy Molasse basin, flysch deposits are overlain by Oligocene to Lower Miocene Molasse sediments (e.g., Burkhard & Sommaruga, 1998; Deville et al., 1994).

The Bornes Massif is a fold-dominated belt where folds strike NE-SW and progressively tighten and rotate counterclockwise moving southward, up to a N-S trend in the southern sector (Figure 1b; e.g., Butler, 1992; Ferrill & Groshong, 1993; Huggenberger & Wildi, 1991). Folded rocks of the internal Bornes are tectonically overlain by Ultra-Dauphinois and Prealpine thrust sheets (Bellahsen et al., 2014) derived from more

internal domains of the Alps, preserved in the Annes and Sulens klippen (e.g., Charollais et al., 1977, 1988). In the Bornes Massif, pre- to syn-orogenic NE-trending longitudinal extensional fault systems affect the Mesozoic and Tertiary succession (Butler et al., 2018; Charollais et al., 1988; Gidon, 1998; Huggenberger & Wildi, 1991; Welbon, 1988; Welbon & Butler, 1992; Villars, 1986) and played a role in controlling fold-and-thrust geometries during alpine compression (Butler et al., 2019; Charollais et al., 1988; Gidon, 1996).

Differently from many fold-and-thrust belt worldwide, where folds are typically detached along thick evaporites overlying crystalline basement rocks (e.g., Sierra Madre Oriental, Lefticariu et al., 2005 and Fischer et al., 2009; Zagros, Lacombe et al., 2011 and Tavani, Storti, et al., 2011; Jura, Laubscher, 1977), in the Bornes Cretaceous limestones are detached from Jurassic rocks along thick Berrasian–Valanginian marls (Bellahsen et al., 2014; Guellec et al., 1990; Mugnier et al., 1996). This feature is documented in the Brizon well (BZN-1 in Figure 1b; Charollais & Jamet, 1990), where the late Jurassic succession is repeated at least three times by folds and thrust slices over a vertical thickness of 2.7 km, whereas Tertiary and Cretaceous rocks are not tectonically duplicated. Ferrill and Groshong (1993) defined the large-scale mechanical stratigraphy of the Mesozoic succession in the region, describing a décollement of structural disharmony in the Berrasian–Valanginian, and a major thrust detachment in the Lower Jurassic rocks. Despite general consensus on this feature, different interpretations were proposed for the structural architecture at depth. In particular, some authors proposed polyharmonic buckle folding in which Jurassic and Cretaceous mechanical units were folded with independent wavelengths in a disharmonic style, without shearing in correspondence of the Berrasian–Valanginian marls and without thrust stacking in the Jurassic rocks (Butler, 1991; Butler et al., 2018; Doudoux et al., 1982; Epard, 1990; Muirhead et al., 2019). Other authors supported a tectonic architecture dominated by thrust-related anticlines in the Jurassic, forming a blind duplex underlying the fold train of Cretaceous limestones, including the Parmelan anticline (Affolter et al., 2008; Bellahsen et al., 2014; Deville & Sassi, 2006; Guellec et al., 1990; Mugnier et al., 1996; Figure 1d).

The Bornes fold train overthrusts the plateau molassique des Bornes along the Subalpine Frontal Thrust, located at the front of the more external anticline (i.e., Parmelan-Montagne de Sous Dine) from surficial geology and interpreted seismic profiles (Charollais et al., 1977; Deville et al., 1994; Guellec et al., 1990; Huggenberger & Wildi, 1991; Mugnier et al., 1996). Evidence for thrusting of the Bornes fold train are exposed along the northeastern side of the Annecy Lake, at Roc de Chere (Figure 1b), where Cretaceous and Tertiary rocks have been commonly interpreted as lying at the footwall of the Veyrier thrust, which tectonically separates them from the overlying Cretaceous succession (Figure 1d; Butler, 1991, 1992; Charollais et al., 1977, 1988; Huggenberger & Wildi, 1991; Martinez, 1976). Further evidence for thrusting of the external Bornes and duplication of Cretaceous rocks come from the Fillière Valley (Figures 2c and 3a), which provides a natural section through the Parmelan anticline and exposes Cretaceous and Tertiary rocks in a tectonic window (Charollais & Liermier, 1967; ; Charollais et al., 1977, 1988; Huggenberger & Wildi, 1991). However, due to very poor exposure, the localization of thrust emergence at the front of the massif remains speculative (Figure 1b). In published geologic (Charollais et al., 1988) and tectonic maps (Butler, 1991, 1992; Huggenberger & Wildi, 1991), the frontal emersion of the thrust is assumed at the tectonic contact between the flysch ("Val D'Illiez Sandstones") and the Molasse (Figure 1b). In the plateau molassique, at 10–12 km from the interpreted emersion of the Subalpine Frontal Thrust, an isolated thrust-related anticline forms the NE-trending topographic elevation of Salève, where Mesozoic and Tertiary rocks (Cretaceous to Oligocene) are exposed (e.g., Deville et al., 1994; Figure 1b). According to Bellahsen et al. (2014), both the Subalpine Frontal Thrust and the thrust that produced the Salève anticline are rooted in the basement (Figure 1d). The involvement of the basement below the Bornes Massif is suggested also by other authors (Guellec et al., 1990; Mugnier et al., 1996).

3. Methodology

A total of 5,963 structural data were collected in 202 field sites, mostly in the Parmelan sector with some additional sites in the Montagne de Sous Dine (the comprehensive list of structural sites and their geographic coordinates are available online at https://data.mendeley.com/datasets/hctvhs5b7d/1). Field work was performed to collect orientation and kinematic data of deformation structures and their crosscutting relationships. We employed orthoimages (ORTHOHR of the Institut National de l' Information Géographique et Forestière IGN-F having a resolution of 20 cm or less) to digitize traces of major faults using ArcGis.

10.1029/2021TC006913

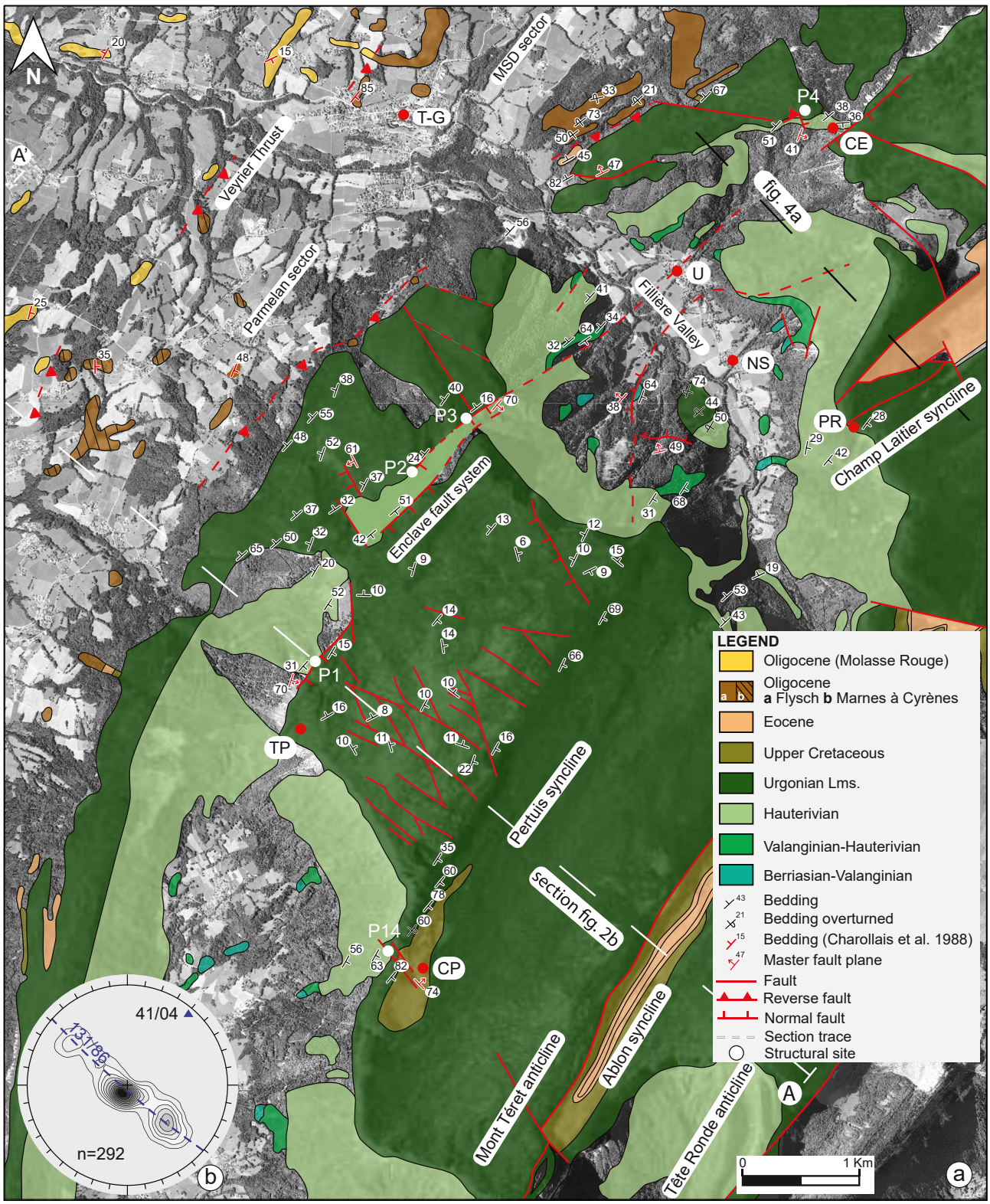

Figure 3. (a) Orthoimage of the study area overlain by a simplified geologic map (modified after Charollais et al., 1988) with selected dip data of bedding planes and major faults. Geographic locations: T-G, Thorens-Glières; CE, Col de l'Enclave; U, Usillon; NS, Nant Sec; PR, Pas du Roc; TP, Tête du Parmelan; CP, Col du Pertuis. MSD sector: Montagne de Sous-Dine sector. P1-14 are structural sites. (b) Stereographic projection with the cumulative contouring of poles to bedding, the best fit cirlcle of contoured data (dashed blue line) and the b-axis (blue triangle); contouring is at 2% intervals. In this and the following figures, stereographic projections are in Schmidt lower hemisphere.

Deformation features are classified in two main groups based on their spatial distribution with respect to major faults (Balsamo et al., 2019): structures documented only in fault-damage zones (i.e., fault-related deformation) and structures occurring in different fold sectors outside fault damage zones (i.e., background deformation). Folding-related deformation structures are classified according to their orientation with respect to the fold axial trend (Storti & Salvini, 1996), namely as transversal (i.e., at high angle to fold axis) and longitudinal (i.e., parallel or sub-parallel to fold axis). The different types of deformation structures are labeled as follows: V = vein, VF = vein in fault damage zone, ST = tectonic stylolite, STF = tectonic stylolite in fault damage zone, CT = conjugate thrust, TF = transversal fault, LF = longitudinal fault. Acronyms for faults, veins and stylolites are always associated with a number that represents their relative chronology with respect to other deformation structures of the same type. It is worth noting that numbers do not stand for tectonic phases and that different types of structures formed in the same tectonic event can have different numbers. Moreover, in the figures veins and stylolites have specific color codes in addition to numbers, to facilitate their visual identification. Background (V and ST) and fault-related (VF and STF) deformation features have different color codes. For the former, V1 veins are orange, V2 veins are green, V3 veins are purple, V4 veins are blue, V5 veins are red, V6 veins are light blue, ST1 stylolites are orange, ST2 stylolites are green, ST3 stylolites are red. For deformation structures in fault damage zones, VF1 veins are black, VF2 veins are dark red, VF3 veins are brown, VF4 veins are gray, STF1 stylolites are dark red, STF2 stylolites are brown, STF3 stylolites are gray. Colors define vein-stylolite associations (e.g., V5 red veins formed at the same time of ST3 red stylolites).

Orientation analysis was carried out with the Daisy3 software (Salvini, 2019). Kinematic/paleostress analysis was performed by WinTensor software, using stylolites as contraction planes (C), veins as tension fractures (T) and conjugate reverse faults as fault planes with slip lines (Delvaux & Sperner, 2003). For paleostress modeling, we used the composite F5 target function that is the most suitable for mixed datasets containing structural elements having different relationships with stress (Delvaux & Sperner, 2003). Structurally compatible associations of veins, stylolites, shear fractures, and faults were used to model stress tensors associated with layer-parallel shortening, syn-folding and post-folding tectonic stages. Four datasets were created by merging data according to their spatial distribution with respect to fold sectors (forelimb, crest and backlimb). Data of deformation structures interpreted as formed before folding were merged after bedding dip removal. For the syn-folding stage, S-C fabrics in the forelimb and backlimb of the Parmelan anticline were used to obtain the orientation of the mean plane containing the mean slip vector on bedding planes as the plane perpendicular to the intersection line between the mean plane of S planes and that of C planes (i.e., tectonic transport direction). In the syn-folding stage, in addition to S-C fabrics also slip directions in bedding-parallel shear veins were taken into account for comparison.

A total of 124 polished thin sections were prepared for petrographic analysis of calcite-filled veins and fault rocks. Thin sections were studied with a Zeiss Axioplan 2 microscope for standard optical petrography, and with a CITL CL Mk5-2 apparatus mounted on a LEICA DM2700P optical microscope for cold cathodoluminescence petrography, performed with operating settings of 250 μA and 10–15 kV. Samples for carbon and oxygen stable isotope analysis (at least 100 μg per sample) were prepared for both syntectonic calcite cements, and Urgonian Limestones and Calcaires gréseux à miches host rocks. Powders from host rock and thick veins were extracted with a dental drill from fresh section cuts. Detailed sampling on thin veins was performed on thin sections by an ESI New Wave Research Micromill. Geochemical analyses were carried out with a Thermo Finnigan DELTA plus XP mass spectrometer coupled with a Thermo Finnigan GasBench II gas preparation and introduction system. Both $\delta^{18}O$ and $\delta^{13}C$ data are referred to the international standard V-PDB. The analytical precision for the carbon isotope determination was 0.10‰ V-PDB and that for the oxygen isotopes was 0.15‰, whereas the prediction uncertainty was c. 0.15‰ for carbon and c. 0.20‰ for the oxygen isotope.

4. Fold Geometry

A peculiar feature of the Parmelan anticline is its flat-topped box-fold geometry (Figures 2a and 2b). The studied sector of the fold, that is the Tête du Parmelan, is located in its central part, where the axis, obtained as the β-pole of bedding, has trend/plunge 041/04 (Figures 1b and 3b). The Parmelan–Montagne de Sous

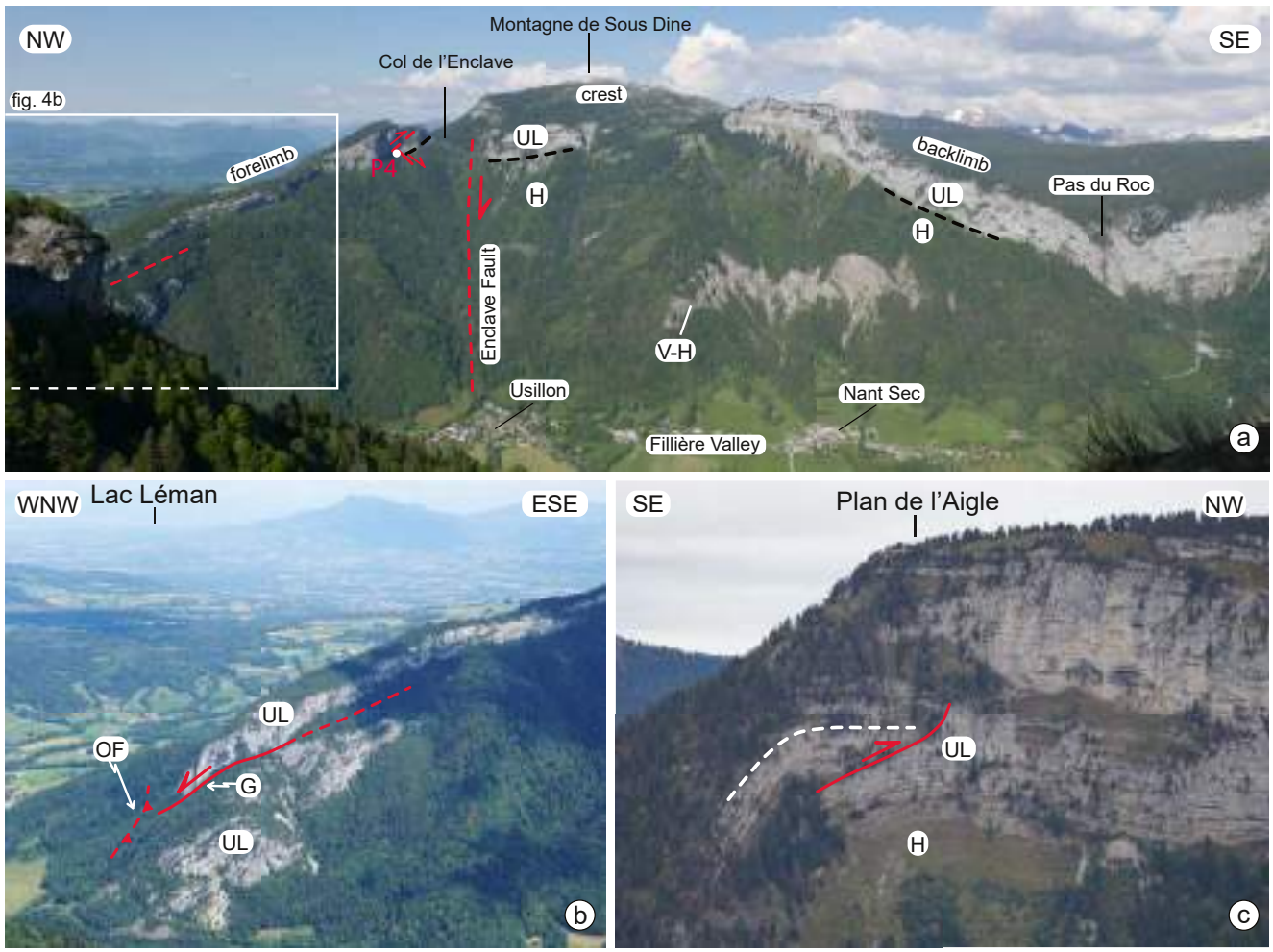

Figure 4. (a) Cross-sectional panoramic view, looking toward NE, of the Fillière Valley transect showing the first order fold geometry of the Montagne de Sous-dine sector, the segment of the Enclave Fault (LF) with the preserved stratigraphic normal offset and the synthetic normal fault in its footwall at structural site P4. (b) Panoramic view of a foreland-dipping fault in the forelimb of the Parmelan anticline (Montagne de Sous-dine sector) that exhibits an extensional kinematics and involves Gault rocks (G) in the footwall overlain by Urgonian Limestones (UL) in the hangingwall (Chevauchement de Pierre Taillée; Charollais et al., 1977, 1988). The Oligocene flysch (OF) in the forelimb of the Parmelan anticline (Montagne de Sous-dine sector) has an overturned geometry. (c) Cross-sectional view, looking toward SW, of the backlimb-crest transition along the Fillière Valley transect showing a top-to-NW reverse fault affecting Urgonian Limestones.

Dine fold sectors have opposite-plunging axes, converging toward the Fillière Valley, which separates the two domains through an axial bump partially preserved on both valley rims (Figure 2c).

In the forelimb of the Parmelan anticline, Urgonian Limestones and Calcaires gréseux à miches dip at 50–60° toward NW (Figures 2b and 3a). Conversely, the overlying Oligocene flysch dips about 30–50° toward SE and has an overturned geometry (Figures 2b and 3a). In the Montagne de Sous Dine, the forelimb includes a low-angle foreland-dipping fault zone that, in the present day orientation, exhibits an extensional kinematics and involves Gault rocks (Upper Cretaceous) in the footwall, overlain by Urgonian Limestones in the hangingwall (Chevauchement de Pierre Taillée; Figures 3, 4a, and b; Charollais et al., 1977, 1988). The forelimb-to-crest transition is localized along the inherited longitudinal extensional Enclave Fault System characterized by overlapping fault segments. Such segments dip ~70° toward SE and juxtapose Urgonian Limestones in the hangingwall against older Calcaires gréseux à miches in the footwall (Figures 3a and 4a).

The anticlinal crest is a ~2 km wide plateau with outstanding exposures of Urgonian Limestones, where bedding surfaces dip <10–15° in different directions (Figures 3a and 4a). The occurrence of subsidiary gentle folds with axis parallel to the main NE-trend of the Parmelan anticline, and of long wavelength

undulations striking oblique to the main structural trend, results in dome-and-basins interference patterns and in a complex surface morphology characterized by culminations and depressions. Transversal fault zones are particularly abundant and well exposed in this sector of the Parmelan anticline (Figure 3a). The transition to the backlimb is more gradual than the crest-to-forelimb one and is characterized by progressively increasing bedding dip angles to values typically reaching 60–70° and becoming locally overturned, as in the Col du Pertuis area (Figure 3a). Folding in the crest-to-backlimb hinge zone is locally accommodated by top-to-NW reverse faulting in the Urgonian Limestones (Figure 4c). Conversely to previous interpretations (Charollais et al., 1988; Huggenberger & Wildi, 1991), we did not find evidence for a major extensional fault system located all along the crest-to-backlimb transition.

5. Structural Data

5.1. Longitudinal Fault Zones (LF)

The Enclave Fault is the most important inherited longitudinal extensional fault system (LF) located along the crest-forelimb transition of the Parmelan anticline. The mean strike of the master fault surface, exposed along the NW face of the Tête du Parmelan at site P1 (Figure 3a), is N22°E and its stratigraphic separation juxtaposes younger Urgonian Limestones against older Calcaires gréseux à miches (Figure 5a). In the hangingwall, Urgonian Limestones are progressively folded in a syncline approaching the master slip surface. In the footwall, Calcaires gréseux à miches strata dip ∼30° toward the SE (Figures 3a and 5a) and are affected by meter-scale subsidiary disharmonic folds (Figure 5b). Fault-parallel stylolites (STF1) occur both in the footwall and hangingwall damage zones (Figure 5c). The preserved fault core is less than one meter thick and consists of fault breccia strongly affected by fault-parallel STF1 stylolites (Figure 5d). Transversal faults (TF1 and TF2) systematically offset the Enclave Fault at this site (Figures 5c and 5e).

At sites P2 and P3, the average strike value of master fault surfaces is N52°E and extensional slickenlines indicate a dip-slip movement (pitch 72°) with a top-to-the-SE sense of shear (Figures 2, 3a, and 5f). In the footwall, Calcaires gréseux à miches strata dip ∼50° toward the SE (Figure 3a). In damage zones, the vein-and-stylolite-dominated deformation pattern is characterized by STF1 stylolites, like at site P1, and by fault-perpendicular sub-vertical calcite-filled VF2 veins (Figure 5f). The latter are widespread in Urgonian Limestones hanging wall strata. In the area of Col de L' Enclave (site P4, Figures 2 and 3a), a well-developed longitudinal extensional fault zone occurs in the forelimb of the Parmelan anticline, striking N29°E and dipping toward the SE with a dip-angle of 41° (Figures 5g and 5i). This fault dissects the Urgonian Limestones- Calcaires gréseux à miches boundary with a top-to-the-SE sense of shear and it is synthetic to the previously described segments of the Enclave Fault. The Calcaires gréseux à miches in the footwall dips ∼30° toward the NNW (Figures 5g and 5i). NE-trending stylolites (STF1) are present in the damage zone and fault core (Figure 5g). When the Calcaires gréseux à miches strata in the footwall are restored to the horizontal (Figure 5h), the master fault dips ∼60° toward the SSE and stylolites become sub-vertical and strike parallel to the master fault.

5.2. Transversal Fault Zones (TF)

A characteristic feature of the Parmelan anticline is the presence of abundant transversal fault zones, well exposed in the flat-lying crestal plateau and clearly identifiable in aerial orthoimages (Figure 3a). Faults traced on the IGN orthoimage can be subdivided into two sets, striking N121E ± 12° (TF1) and N153E ± 11° (TF2), respectively. TF1 faults are more persistent and, in many cases, they are abutted by TF2 faults (Figure 6). Transversal fault zones dissect both fold limbs and their offsets range between a few and a hundred meters. Stratigraphic separations are difficult to quantify in the crestal domain, due to the absence of suitable markers, but tens of meters of offset have been observed for both TF1 and TF2 on the NW-SE trending natural cross-section provided by the Fillière Valley.

The structural architecture of TF1 and TF2 fault zones typically consists of <10 m thick damage zones dominated by stylolite and vein assemblages (Figures 6, 7a, and b) and by centimeter- to decimeter-thick fault cores consisting of cohesive monogenic protocataclasite cemented by calcite (Figure 7c). In many TF1 and TF2 damage zones (9 out of 13), fault-parallel veins occur (VF1) (Figure 7a). VF1 veins are typically cross-cut by two vein-stylolite associations orthogonal to bedding and oblique to master fault planes; some

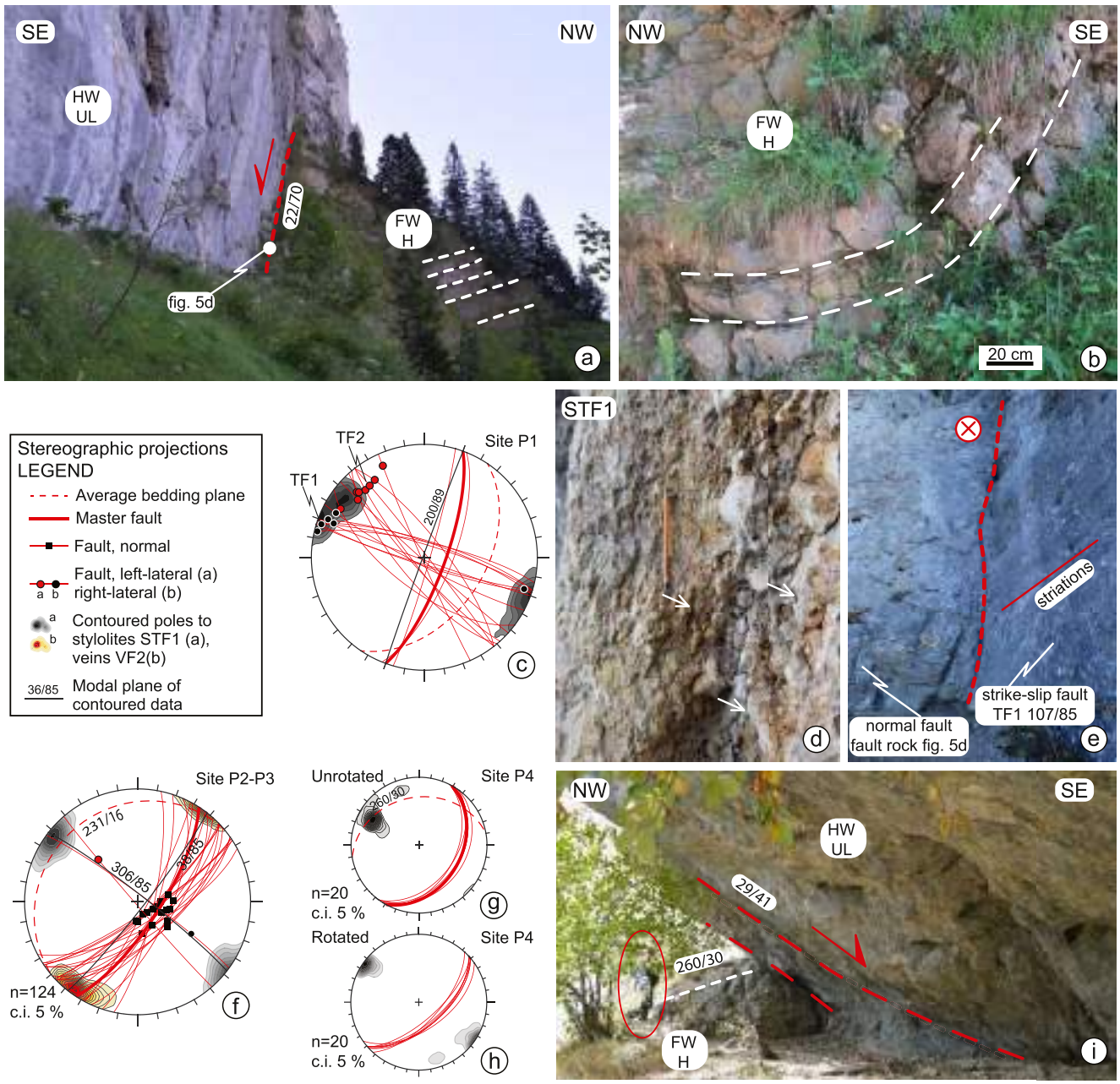

Figure 5. Outcrop images and structural data collected along longitudinal extensional faults (LF). (a) Extensional fault at site P1 with the preserved stratigraphic normal offset (i.e., young-over-old rocks). HW UL: hanging wall Urgonian Limestones; H FW: Hauterivian Calcaires gréseux à miches foot wall. (b) Subsidiary folds in Calcaires gréseux à miches strata in the footwall of the master Enclave Fault (c) Stereographic projection of structural data at site P1. (d) Cataclastic fault core of the Enclave Fault at site P1. White arrows indicate sub-vertical stylolites striking parallel to the master fault (STF1) and affecting its fault core. (e) Example of intersection between longitudinal (LF) and transversal (TF) faults. In the image, the Enclave Fault (LF) is dissected by a WNW-ESE transversal fault (TF1) with a right-lateral displacement at site P1. Dashed red line for TF1. Red line for the orientation of the striations on TF1 master slip surface. (f) Stereographic projection of structural data at site P2 and P3 (see stereographic projections legend for details). (g–h) Stereographic projection of structural data at site P4. (i) Synthetic normal fault in the footwall of the master Enclave Fault at site P4. The master fault plane makes an angle of ~70° with bedding planes in the foot wall (dashed white line).

of them underwent brecciation and re-cementation (Figures 7a and 7d). Assemblage (a) is characterized by ~E-W striking STF2 stylolites (N85°E, 83°S) and NNW-SSE striking VF3 veins (N157°E, 88°E), indicating right-lateral kinematics on both TF1 and TF2 master slip surfaces (Figure 6b). Assemblage (b) is characterized by NNE-SSW STF3 stylolites (N12°E, 86°E) and ~E-W VF4 veins (N93°E, 88°S), indicating left-lateral

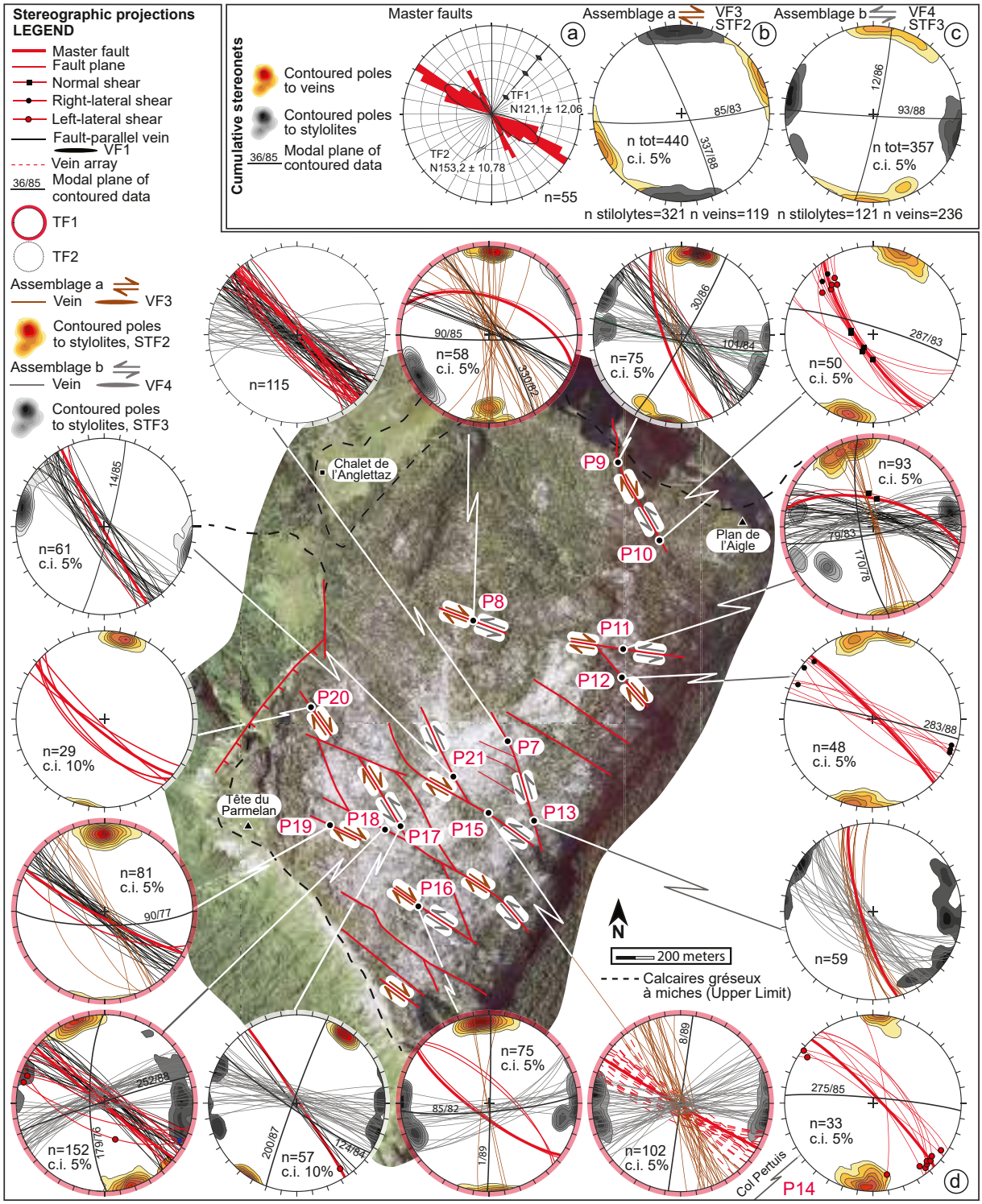

Figure 6. Stereographic projections of structural data (master slip surfaces, slickenlines, stylolites and veins) collected in the damage zones of transversal fault zones (TF1 and TF2) at structural sites P8-P16. (a) Cumulative rose diagram showing fault strikes for both TF1 and TF2 (azimuth data from IGN orthophoto). In the diagram, the Parmelan anticline fold axial trend is also shown for reference. (b–c) Cumulative stereographic projections of veins-and-stylolites assemblages foboth TF1 and TF2: assemblage a (VF3-STF2) and assemblage b (VF4-STF3), respectively. See text for details. (d) Stereographic projections of structural data collected on transversal faults (see stereographic projections legend for details). Contour intervals and data numbers are indicated inside the stereonets.

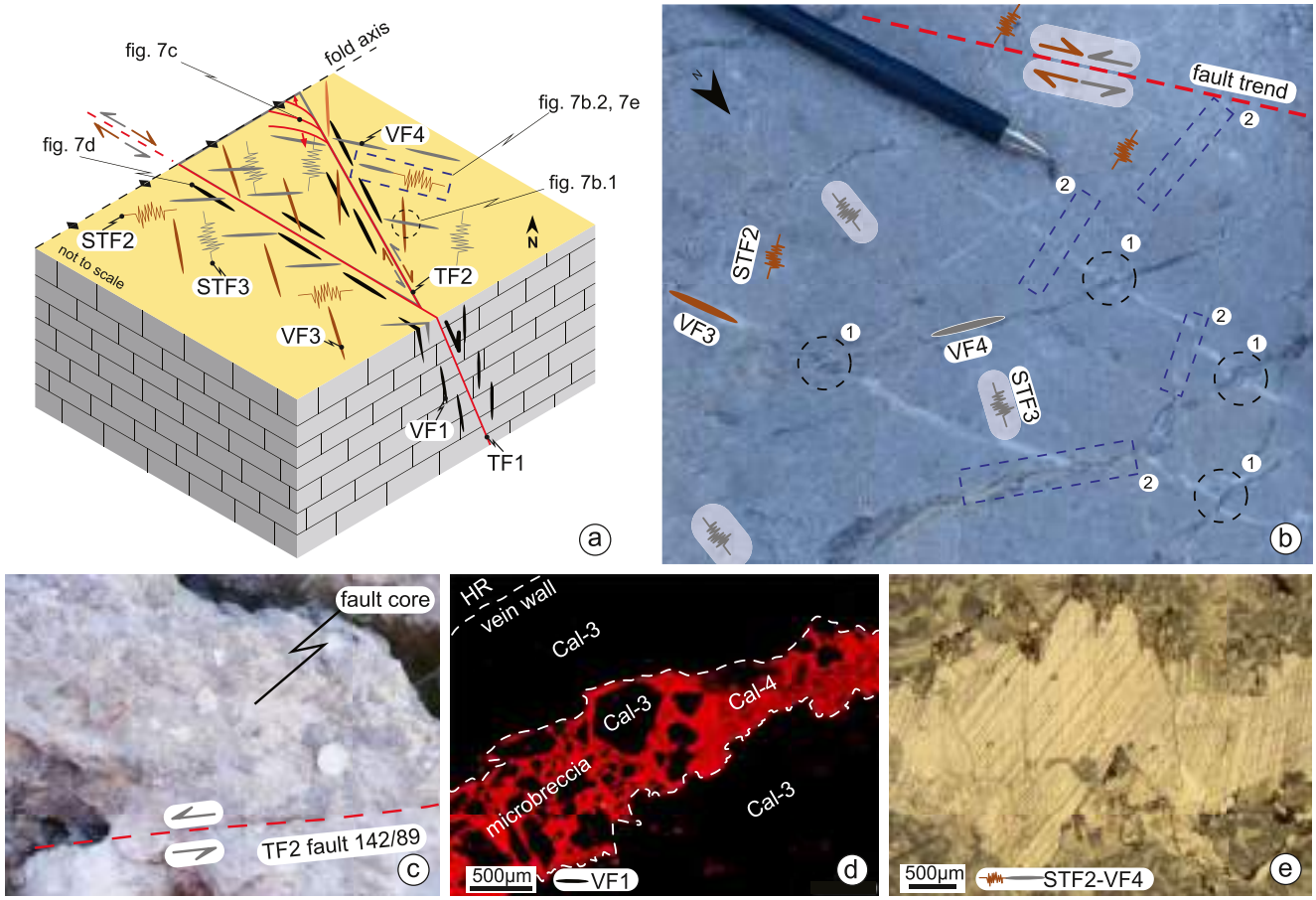

Figure 7. Schematic sketch (a) and outcrop image (pavement; b) showing the orientation and the relative chronology of deformation features (veins and stylolites) in transversal fault damage zones. The image in (b) is an example of a TF2 fault damage zone (structural site P9). Numbers (1–2) and the associated dashed lines (black-blue) highlight cross-cutting relationships between different deformation structures. (c) Outcrop image illustrating an example of cataclastic fault core. The sample is from a TF2 fault (structural site P7). (d) CL image showing an example of a fault-parallel VF1 vein that underwent brecciation and re-cementation. The sample is from a TF1 fault damage zone (structural site P19). (e) PPL image showing an example of dilated STF2 stylolite filled by calcite cement and forming a VF4 vein.

kinematics on both TF1 and TF2 master slip surfaces (Figure 6c). Actually, in six fault damage zones out of thirteen (sites P8, P11, P16, P17, P18, P9 in Figure 6d) we recognized both assemblages, indicating that reactivation with opposite shear senses was quite common in transversal fault zones. Cross-cutting relationships always indicate that right-lateral strike-slip shearing was subsequently overprinted by left-lateral kinematics (Figures 7a and 7b) when both new veining and dilation of pre-existing stylolites occurred, with calcite precipitation along them (Figure 7e).

5.3. Background Deformation

In the forelimb of the Parmelan anticline, far from fault zones, different associations of mesostructures and their relative chronology are exposed, both in the Urgonian Limestones and in the underlying Calcaires gréseux à miches (Figure 8). NNW-trending bed-perpendicular veins (V1) become vertical after restoration of bedding to the horizontal (Figures 8f and 8g) and are associated with scarce bed-perpendicular ST1 stylolites. Both the Urgonian Limestones and the Calcaires gréseux à miches are affected by NE-SW striking subsidiary fault sets (CT) with well-preserved calcite slickenfibers, characterized by dihedral angles of ~50° and decimetric offsets (Figures 8h and 8i). In the present orientation, low angle NW-dipping faults have an extensional kinematics whereas those dipping at high angle toward NW exhibit a contractional kinematics (Figure 8a). The two CT fault sets are associated with ST2 stylolites and bed-parallel calcite-filled veins (V2), characterized by mutual cross-cutting relationships (Figures 8c, and 8h–8j). When bedding is

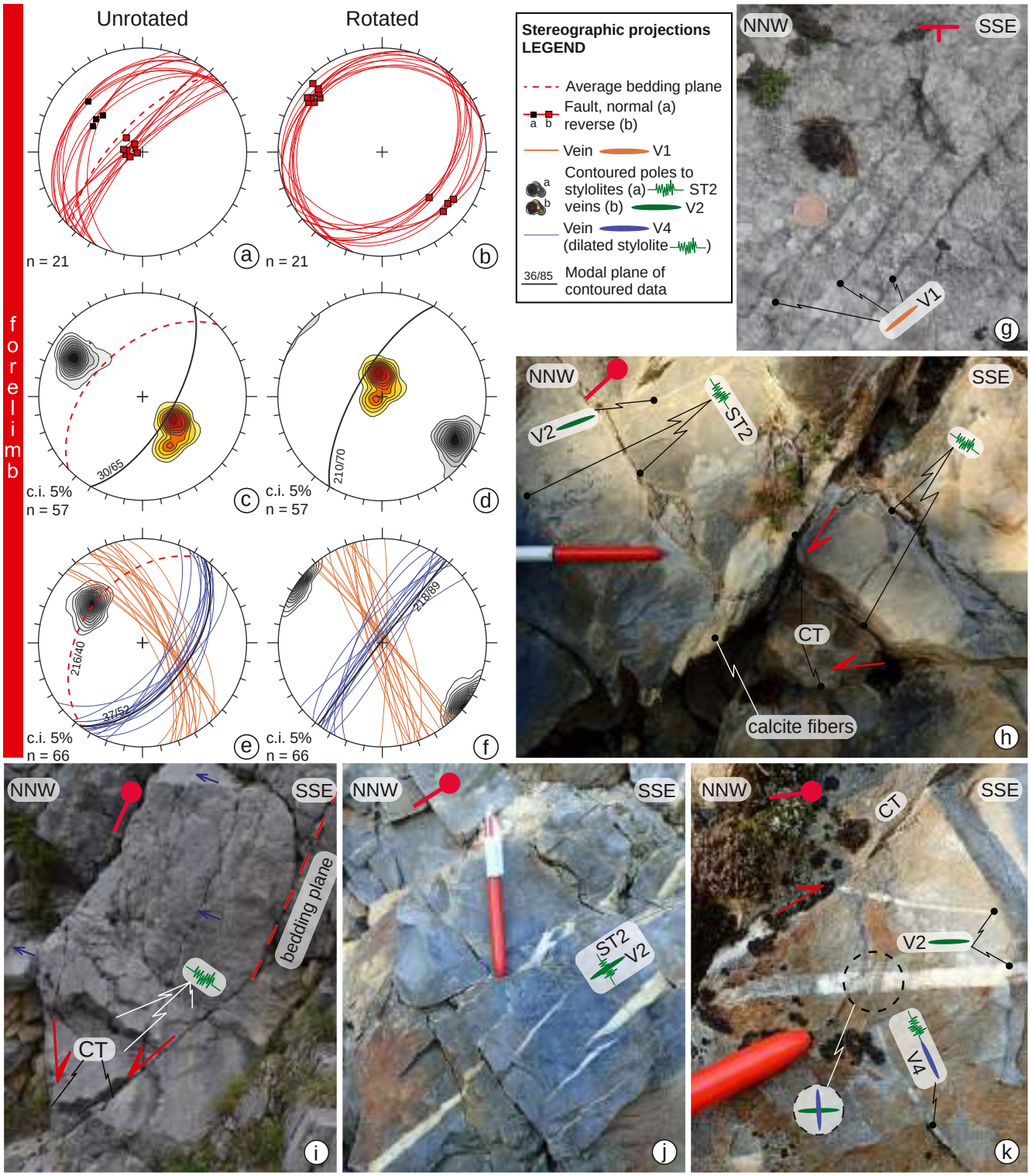
Unrotated
Rotated
foreli mb
n = 21
a
n = 21
b
30/65
c.i. 5%
n = 57
c
210/70
c.i. 5%
n = 57
d
216/40
37/52
c.i. 5%
n = 66
e
218/89
c.i. 5%
n = 66
f
Stereographic projections
LEGEND
Average bedding plane
Fault, normal (a)
reverse (b)
Vein V1
Contoured poles to
stylolites (a) ST2
veins (b) V2
Vein V4
(dilated stylolite)
36/85 Modal plane of
contoured data
NNW
SSE
V1
g
NNW
SSE
V2
ST2
CT
calcite fibers
h
NNW
SSE
bedding plane
CT
i
NNW
SSE
ST2
V2
j
NNW
SSE
CT
V2
V4
k

Figure 8.

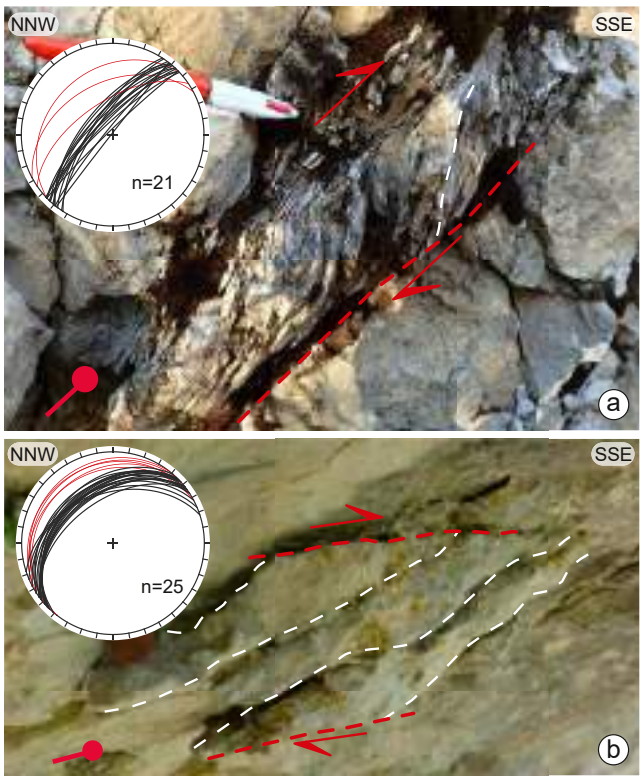

Figure 9. Outcrop images and stereographic projections of SC-type shear fabrics in the forelimb of the Parmelan anticline, occurring in pelite-rich interlayers of the Calcaires gréseux à miches (a) and in Urgonian Limestones beds (b). They both suggest a top-to-the-hinge sense of shear. In the outcrop images, dashed red and white lines represent C- and S-surfaces, respectively. In the stereographic projections, red and black circles indicate C and S planes, respectively.

rotated to the horizontal, this structural assemblage consists of two sets of NE-trending, conjugate CT low-angle contractional faults bisected by sub-horizontal veins (V2) orthogonal to NE-trending sub-vertical ST2 stylolites (Figures 8b and 8d). In some cases, ST2 stylolites have been dilated and sealed by calcite cements, forming millimetric veins (V4) cross-cutting the pre-existing bed-parallel ones (Figures 8e, 8f, and 8k). Both formations show S-C type arrays indicating top-to-the-crest layer-parallel shearing (Figure 9).

In the crestal plateau of the Parmelan anticline, the background deformation pattern is comparable with that observed in the forelimb (Figure 10). Calcite-filled vertical veins trending NNW-SSE (V1) are abundant and are typically organized in clusters of type-2 en-echelon arrays (Srivastava, 2000) overprinted by bedding-parallel stylolites (Figures 10a, 10i, and 10j). Such arrays indicate both left- and right-lateral shearing, being the azimuth of the latter quite scattered compared with that of the former (Figures 10b and 10c). The length of NNW-SSE (V1) veins commonly does not exceed 30–40 cm, the vertical persistence is limited to a few tens of cm, and the aperture is mostly lower than 1 cm (Figure 10j). Multiple syntaxial opening events sealed by different calcite cements are common (Figures 10i, 11a, and 11b). ENE-WSW trending, bed-perpendicular stylolites are associated with V1 veins (Figure 10a). NE-SW trending thrusts (CT), both NW- and SE-dipping and with calcite slickenfibers are widespread (Figures 10d, 10k, and 10l). They are associated with bedding-parallel calcite veins (V2) and near vertical NNE-SSW trending longitudinal tectonic stylolites (ST2; Figures 10e and 10f). When the gently dipping bedding is restored to the horizontal, ST2 tectonic stylolites become vertical and trend NE-SW (Figure 10g). Local concentrations of NE-SW trending longitudinal veins (V4) occasionally occur in the anticlinal crestal plateau. No overprinting relationships have been observed and this prevents to infer a relative chronology with the previously described deformation structures. The abundance of V4 veins increases in the transitional domain between the flat-lying crest and the backlimb, where bedding dips toward SE. In the crest, all the previously described deformation structures (i.e., V1 and V2 veins, ST2 stylolites and CT reverse faults) are overprinted by ~E-W veins (V5) crosscutting bed-parallel stylolites, and by ~N-S stylolites (ST3; Figures 10h, 10j, 10m, and 11c). V5 veins are typically thicker and longer than NNW V1 ones (Figures 10h and 11a). N-S stylolites (ST3) are commonly infilled by calcite cement (V6) that cross-cuts E-W V5 ones (Figures 11d and 11e).

In the backlimb, the background deformation pattern is comparable with that observed in the forelimb (Figure 12). NNW-SSE trending, steeply dipping veins (V1) and associated, less abundant ENE-WSW trending stylolites (ST1) occur (Figures 12a and 12b). Upon bedding dip removal, V1 veins become bed-perpendicular, with a NNW-SSE azimuthal trend that makes an acute angle with respect to the fold axis (Figure 12a). Urgonian Limestones are also affected by NE-SW trending thrusts (CT) and by gently NW-dipping stylolites (ST2; Figure 12b). Upon bedding dip-removal, ST2 stylolites become sub-vertical and trend NE-SW (Figure 12c). Similarly, in the underlying Calcaires gréseux à miches, NE-SW striking ST2 stylolites are abundant in the more carbonate-rich strata and become vertical when bedding is rotated to the horizontal

Figure 8. Stereographic projections and outcrop images of the background deformation pattern in the forelimb of the Parmelan anticline. Examples are from Urgonian Limestones and Calcaires gréseux à miches. (a–f) Stereographic projections of structural data (veins, stylolites and faults with slickenfibers) in their present day orientation (a–c–e) and after bedding dip removal (b–d–f). (g) Plan-view of an Urgonian Limestones bedding surface showing V1 veins. (h) Cross-sectional view of Calcaires gréseux à miches strata illustrating CT faults with calcite fibers, ST2 stylolites and V2 veins. (i) Cross-sectional view of Urgonian Limestones strata illustrating CT faults and ST2 stylolites. Blue arrows indicate bedding-parallel compaction stylolites. Dashed red line for bedding plane. In this and in the following figures the red dot with the associated red line segment indicates bedding dip angle. (j) Cross-sectional view of Calcaires gréseux à miches strata illustrating ST2 stylolites, V2 veins and their mutual cross-cutting relationships. (k) Cross-sectional view of Calcaires gréseux à miches strata illustrating CT faults with calcite fibers, V2 veins and V4 veins (dilated ST2 stylolites). In the dashed black circle cross-cutting relationship between V2 and V4 veins.

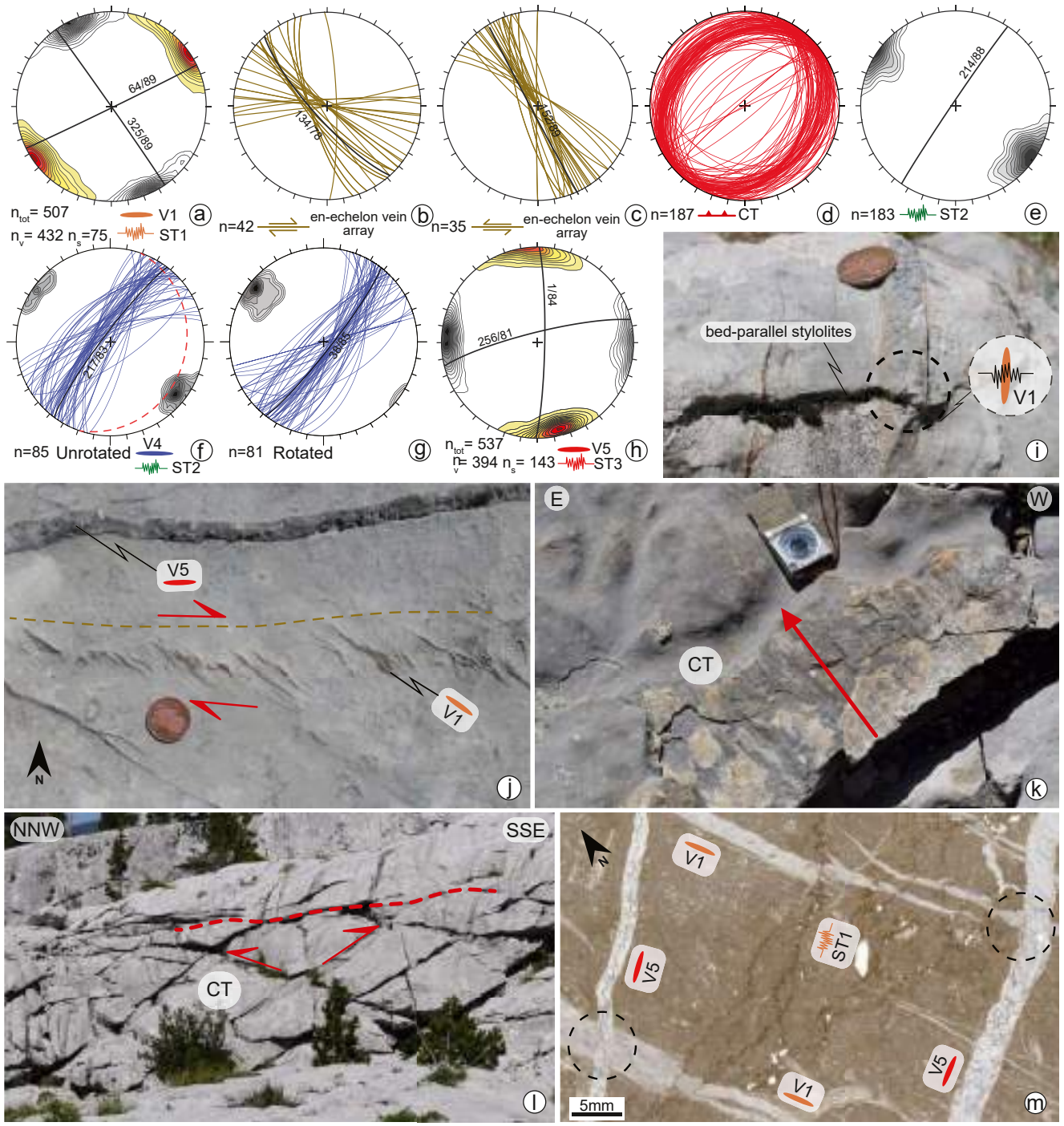

Figure 10. Stereographic projections, outcrop images and thin section scans of the background deformation pattern documented in the crest of the Parmelan anticline. Examples are from Urgonian Limestones. (a–h) Stereographic projections of structural data: red and brown circles represent CT faults and V1 array trends, respectively; blue circles represent V4 veins; gray-scale and orange-scale contours are contoured poles to stylolites and veins, respectively. (i) Cross-sectional view showing the cross-cutting relationship between V1 veins and bedding-parallel compaction stylolites. The black dashed circle indicates the intersection point. Note the two generations of calcite filling V1 vein visible to the naked eye thanks to their difference in color. (j) Pavement-view showing an example of V1 veins organized in an en-echelon array and of V5 veins. The dashed brown line indicate the array trend. The geometrical arrangement of the V1 veins into the array suggests a right-lateral shear sense. (k) Plan-view of a CT fault slip surface with well-preserved calcite slickenfibers suggesting a top-to-SE sense of movement. (l) Cross-sectional view of Urgonian Limestones strata deformed by a network of CT faults. (m) Oriented double-polished section scan showing V1 veins, ST1 stylolites, V5 veins and their cross-cutting relationships. The dashed black circles indicate the V1–V5 intersection points.

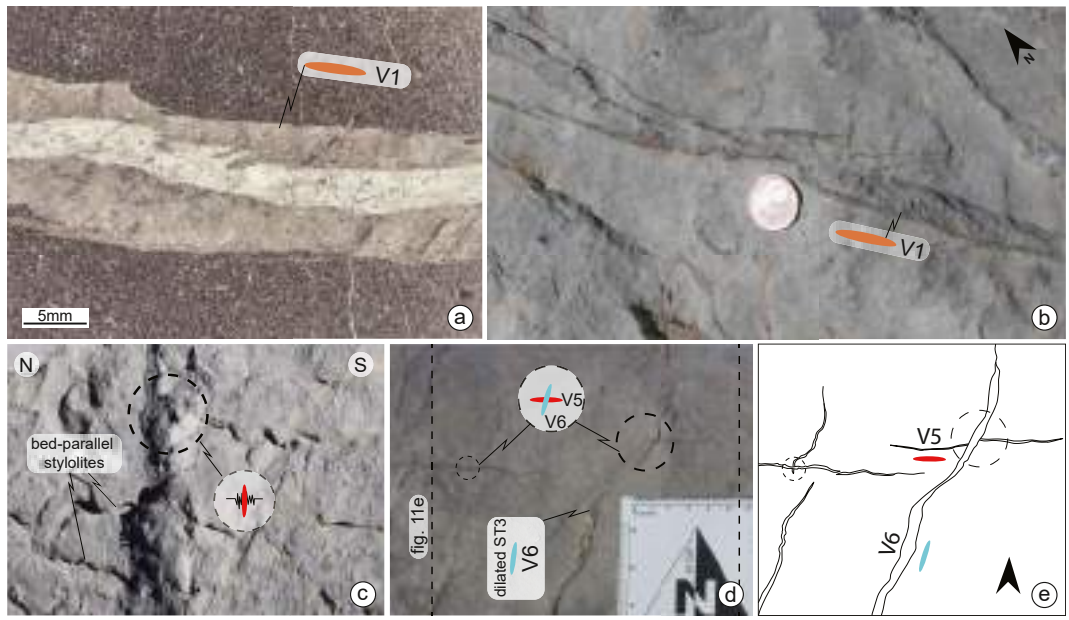

Figure 11. Outcrop images and thin section scans of the background deformation pattern documented in the crest of the Parmelan anticline. (a) Thin section scan of a V1 vein cemented by fibrous calcite crystals. Note the subsequent reopening and infilling by blocky calcite crystals visible in the vein core. (b) Pavement-view of a V1 vein infilled by two different calcite generations: an older yellowish one visible at the vein rims reopened by a younger greyish one in the core of the vein. (c) Cross-sectional view of a V5 vein cross-cutting bedding-parallel compaction stylolites. Example of intersection point in the black dashed circle. (d–e) Pavement-view of V5 and V6 veins (dilated ST3 stylolites), and their cross-cutting relationships; intersection point in the black dashed circle.

(Figures 12d–12f). Subsidiary CT reverse faults are abundant and displace bedding with centimetric to metric offsets (Figure 12f). Pelitic interlayers are affected by an intense slaty cleavage sub-parallel to bedding and by bedding-parallel calcite veins (V3) with dip-slip slickenfibers indicating top-to-NW shearing (Figures 12d and 12g). Urgonian Limestones are affected by discrete domains where meter-thick shear zones with S-C-type fabrics developed, indicating top-to-the crest (NW) slip (Figure 12h). S-surfaces are pressure solution seams that dip toward SE and make an angle of ~45° with respect to C-surfaces, which originated from sheared bedding (Figure 12h). The abundance of NE-SW V4 longitudinal veins decreases in the backlimb with respect to the crest-backlimb transition. These veins commonly originated by dilation of bed-perpendicular stylolites and have decimetric length and millimetric aperture (Figure 12a).

6. Petrography and Geochemistry of Calcite Cements

Petrographic analysis supports field evidence of multiple generations of calcite cements filling tectonic veins. Calcite infillings of background veins can be subdivided in five major groups (Cal-1 to 5). Cal-1 can be further split in two subgroups: Cal-1a and Cal-1b. Cal-1a consists of "dirty" elongated to fibrous calcite crystals that are mostly orthogonal to vein walls (Figures 13a and 13b). Crystals have high length-width ratios (4–10) and are intensively affected by twinning. Crack-seal microstructures such as host-rock inclusions trails (Bons et al., 2012) are present. Cal-1b occurs as blocky, equidimensional "dirty" rhombohedric crystals frequently twinned. Under CL light, both Cal-1a and Cal-1b are dull to nonluminescent and exhibit the same CL response of the host rock (Figure 13c). Calcite cements in calcite slickenfibers of CT faults were not add to any calcite group because of their complex internal microstructures that do not allow to recognize uniform crystal morphologies. However, since they exhibit under CL light the same response of Cal-1a and Cal-1b (i.e., dull luminescence), very similar to that of the host rock, these cements have been grouped into a Cal-1 "type" generation for their affinity with Cal-1 cements. Cal-2 consists of blocky calcite spanning from 200 μm to 8 mm in size, with a "clean" appearance; about 50% of the crystals are twinned (Figures 13a and 13b). Vein texture is frequently non-equidimensional, with smaller scalenohedral crystals close to the vein walls and bigger crystals at the vein center, indicating growth competition (Bons et al., 2012). Under

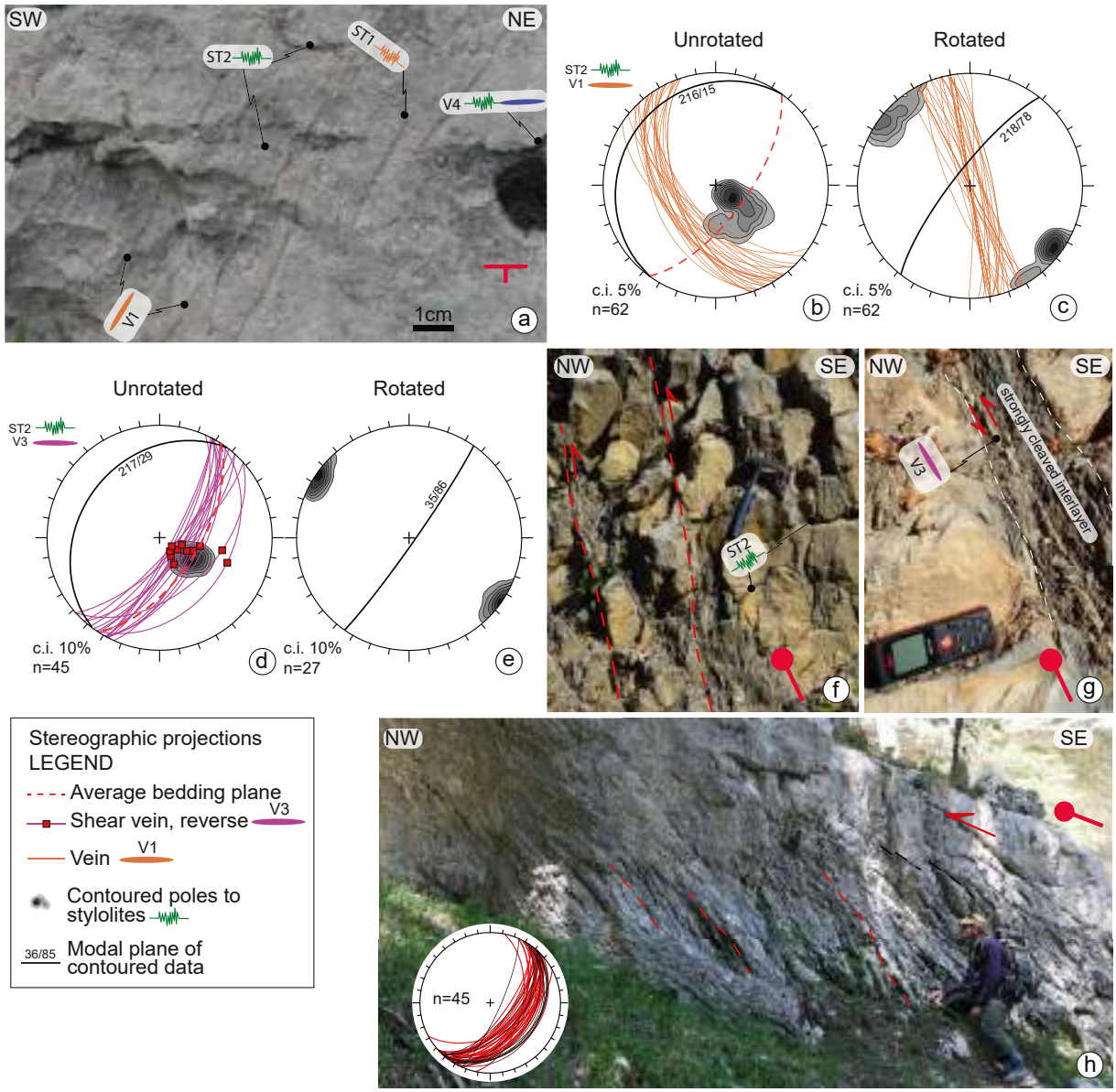

Figure 12. Stereographic projections and outcrop images of the background deformation pattern documented in the backlimb. (a) Plan-view of an Urgonian Limestones bedding surface showing V1, V4, ST1, and ST2. (b–e) Stereographic projections of structural data in their present day orientation and after bedding dip removal. Since bed-parallel V3 shear veins become sub-horizontal after bedding dip removal, they are not reported in the stereographic projection in (e). (f) Cross-sectional view of Calcaires gréseux à miches strata displaying bed-perpendicular ST2 stylolites and subsidiary reverse faults (CT) offsetting bedding surfaces. (g) Cross-sectional view of Calcaires gréseux à miches strata showing an example of V3 shear veins sub-parallel to bedding. Note the pervasive cleavage in the pelite-rich interval. (h) Outcrop image and stereographic projection of an example of a meter-thick shear zones with S-C-type fabrics indicating top-to-the crest (NW) slip.

CL light, Cal-2 is usually brighter than Cal-1a/b and shows nonsystematic faint variations in luminescence inside the crystals, from dull to pale orange, irregularly following crystal growth zones (Figure 13c).

An equant to inequant granular vein texture with moderately twinned to untwinned crystals having dimensions of 500 μm to 4 mm, characterizes vein sets infilled by Cal-3 cements (Figures 13d and 13f). Under CL light, Cal-3 crystals have irregular patterns with intra-crystalline sector zonations ranging from brown to pale orange colors (Figure 13e). An additional calcite cement generation occurs in the studied background veins (Cal-4) and is much less abundant than the previous ones. On the other hand, Cal-4 typically cements fault-rocks and related veins. It consists of small (50–200 μm) granular anhedral brownish crystals that,

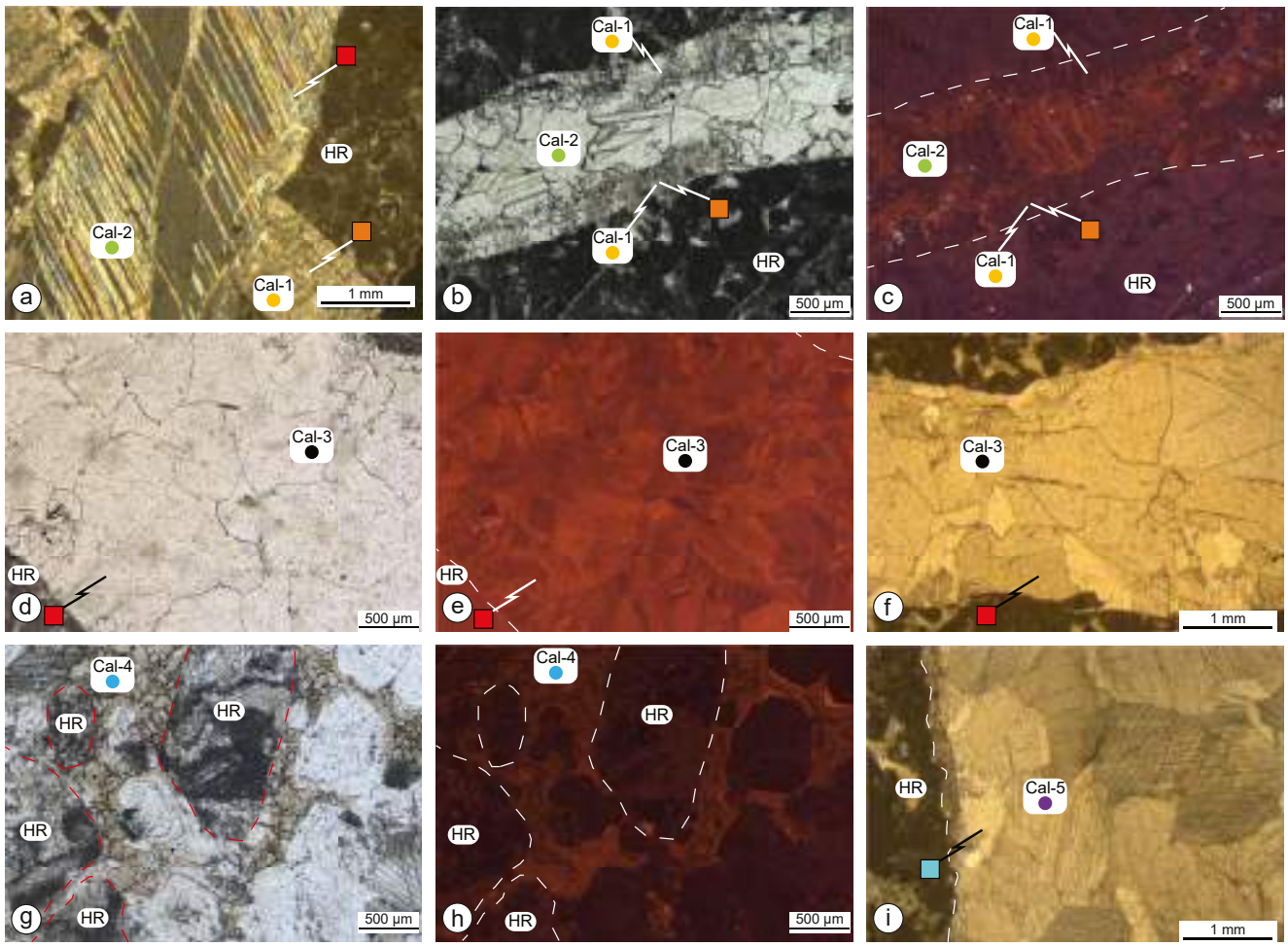

Figure 13. Photomicrographs of examples of calcite cements filling tectonic veins. Symbols indicate both the vein set and the calcite cement generation (see legend in Figure 14). (a) Example of an intersection point amongst a V1 and a V5 vein under cross-polarized light. Note the different vein texture: the V1 vein is filled by fibrous and "dirty" Cal-1 crystals whereas the V5 vein by vein-sized twinned Cal-2 crystals. In this and in the following images HR stands for host rock. (b and c) V1 vein displaying Cal-1 crystals near the vein wall and Cal-2 crystals postdating it under plane-polarized light (PPL) and in the corresponding cathodoluminescence (CL) image, respectively. The white dashed lines indicate the vein-host rock boundaries. (d and e) V5 vein filled by Calc-3 under PPL light and in the corresponding CL image, respectively. The white dashed lines indicate the vein-host rock boundaries. Note the intra-crystalline sector zonations in the CL image. (f) V5 vein filled by Cal-3 under PPL. (g and h) Cohesive monogenic fault breccia representing an example of transversal fault (TF) fault core in PPL and in the corresponding CL image. Rounded fragments of Urgonian Limestones host rocks (delimited by dashed red and white lines) are cemented by calcite crystals. Note the texture and the bright luminescence of Cal-4. (i) PPL image displaying an example of V6 vein filled by Cal-5.

under CL light, show brighter orange luminescence compared to Cal-1 to 3 (Figures 13g and 13h). Finally, Cal-5 consists of "dirty" equidimensional blocky crystals moderately twinned to untwinned, having millimetric size that, under CL light, are non-luminescent (Figure 13i).

Carbon and oxygen stable isotope data from host rocks, background and fault-related veins, fault-rocks, and slickenfibers, are summarized in Figure 14. Urgonian Limestones host rocks including bioclasts, cements, and matrix have $\delta^{18}O$ values ranging from −2.26‰ and −6.04‰ and $\delta^{13}C$ values between 3.28‰ and −1.56‰. These isotopic values do not fit neither into the field of calcite in equilibrium with Cretaceous seawater (Veizer et al., 1999) nor with the Urgonian marine calcite (Moss & Tucker, 1995). Cal-1 and Cal-1 "type" cements have $\delta^{18}O$ values ranging from −0.72‰ to −8.81‰ and $\delta^{13}C$ values between 2.64 ‰ and −0.20 ‰, both in the range of the Urgonian Limestones host rocks. Cal-2 cements have $\delta^{18}O$ values ranging from −8.60 ‰ to −16.20 ‰ and $\delta^{13}C$ values between 6.34‰ and 0.31‰. Cal-3 cements have $\delta^{18}O$ values ranging from −9.62‰ to −16.12‰ and $\delta^{13}C$ values between −0.37‰ and −4.45‰. Cal-4 cements have $\delta^{18}O$ values ranging from −11.44‰ to −13.58‰ and $\delta^{13}C$ values between −4.03‰ and −5.16‰. Cal-5 cements

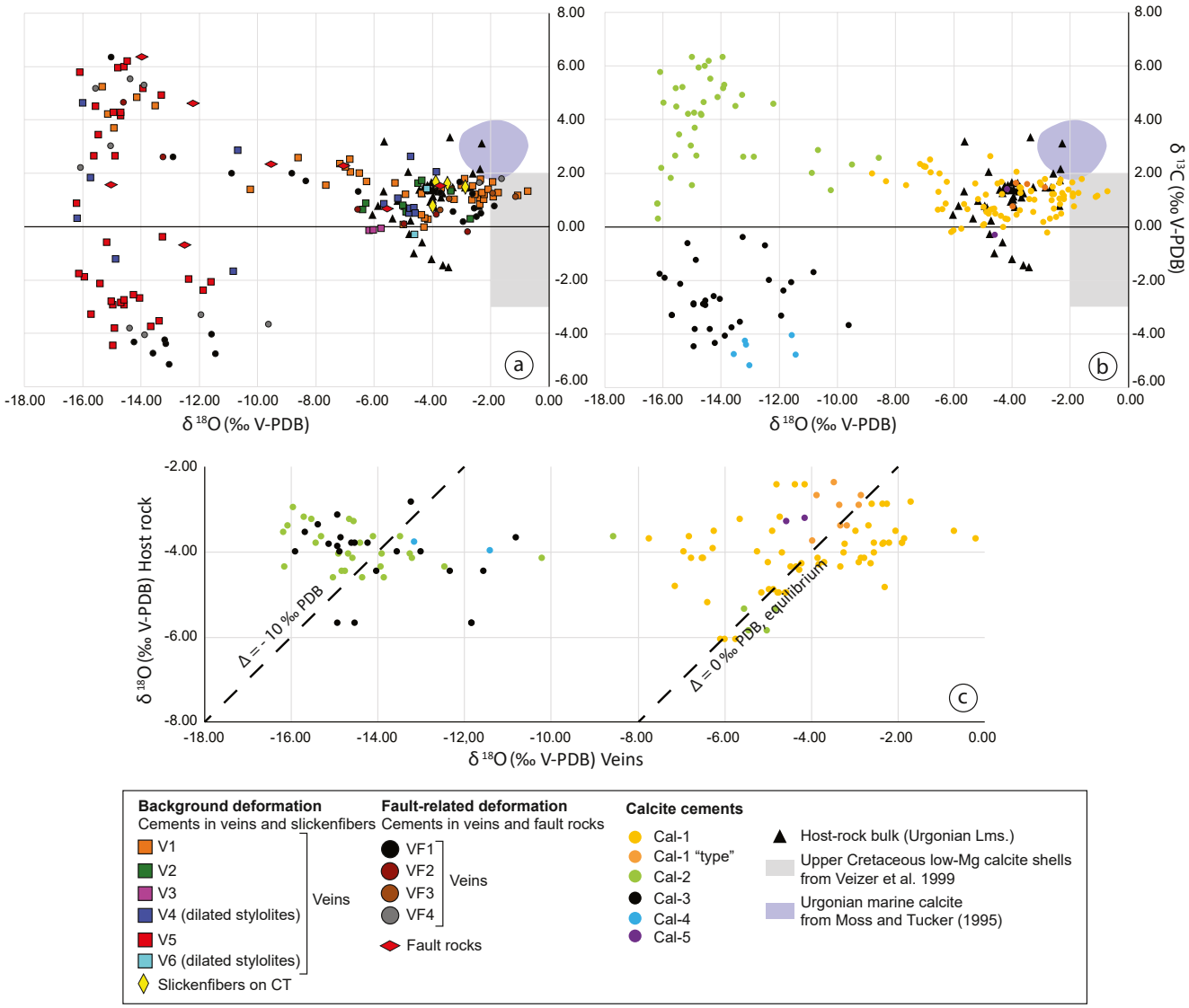

Figure 14. Stable isotope data (C and O) of calcite cements in tectonic veins, slickenfibers and fault rocks. See the legend for details. Colored fields indicating the ranges of Upper Cretaceous marine calcites (after Veizer et al., 1999) and of Urgonian marine calcites (Moss & Tucker, 1995) are also shown for reference. V-PDB stands for Vienna Pee Dee belemnite (a) Data classified according to their structural set. (b) Data classified according to their petrographic attribution (Cal-1/5). (c) $\delta^{18}O$ of veins versus $\delta^{18}O$ of related host-rocks.

have $\delta^{18}O$ values ranging from −4.18‰ to −4.60‰ and $\delta^{13}C$ values between 1.42‰ and 0.29‰, both in the range of the Urgonian Limestones host rocks.

7. Structural, Petrographic, and Geochemical Summary

The structural complexity of deformation pattern, crosscutting relationships, and vein-filling cements, is schematically summarized in Figure 15. The oldest veins documented in the background deformation pattern are NNW-SSE trending, bed-perpendicular V1 veins, oriented at high angle to the fold axial trend. They are widespread in the anticline and are frequently organized in en-echelon arrays (i.e., type 2 en-echelon arrays (Srivastava, 2000). V1 veins are filled by Cal-1 and Cal-2 cements and are cross-cut by bed-parallel stylolites. ENE-WSW trending, bed-perpendicular ST1 tectonic stylolites occur in the crest and in the limb and are perpendicular to V1 veins. V1 and ST1 are overprinted by conjugate faults CT, and coeval bed-parallel V2 veins and bed-perpendicular ST2 stylolites, occurring both in the limbs and in the crest. Removing bedding dip produces longitudinal thrust-backthrust conjugate pairs bisected by horizontal veins and associated

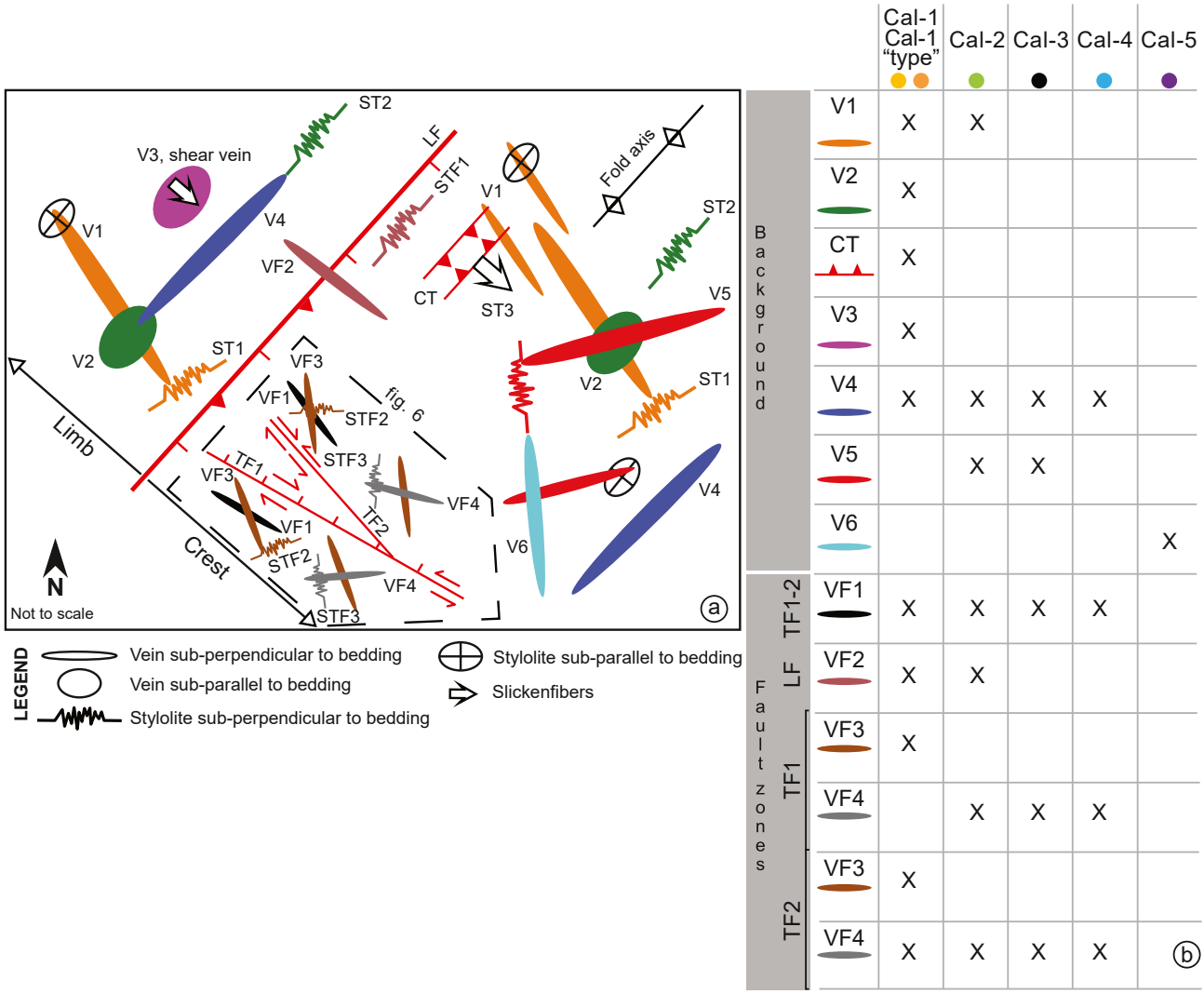

Figure 15. Structural, petrographic and geochemical summary. (a) Schematic sketch in map-view showing the average orientations of background and fault-related deformation structures and their cross-cutting relationships. The sketch is subdivided in crestal and limb sectors, with the latter being representative of both forelimb and backlimb. The azimuthal trends of major transversal (TF1-2) and longitudinal (LF) fault zones, and of the Parmelan fold axis are also shown. (b) Cross-table of vein sets and the corresponding calcite cements. The existence of more than one cement generation on a vein set in the cross-table does not necessarily mean that all these generations coexist on single veins. The vein list is divided in background and fault zones. Symbols indicating calcite cements are as in Figure 14.

longitudinal vertical ST2 stylolites. Calcite slickenfibers on CT faults pertain to Cal-1 "type" cements and V2-V3 veins are infilled by Cal-1. The latter are bedding-parallel shear veins with calcite slickenfibers indicating top-to-the-hinge reverse shearing both in the forelimb and in the backlimb. V2 veins are cross-cut by V4 bed-perpendicular longitudinal ones, which also dilate ST2 stylolites. V4 veins mostly occur in the crest-to-limb transitional domains and are filled by multiple generations of calcite (Cal-1 to Cal-4; Figure 15b). The stratabound geometry of V2, ST2, and V4 prevents development of overprinting relationships with V3 veins, which are typically confined into the marly interlayers. In the crest of the anticline, ~E-W trending, bed-perpendicular V5 veins occur, associated with ~ N-S trending ST3 tectonic stylolites. V5 systematically cross-cut V1 and V2 veins and are filled by Cal-2 and Cal-3 cements (Figure 15b). The younger deformation structures occurring far from fault damage zones are V6 veins filled by Cal-5 cements, which are confined to the crest and commonly dilate ST3 stylolites.

Longitudinal fault damage zones (LF) are characterized by the presence of abundant fault-parallel STF1 stylolites and associated fault-perpendicular VF2 vertical veins filled by Cal-1 and Cal-2 cements

(Figure 15). Transversal TF1 and TF2 fault damage zones contain more complex deformation patterns that include fault-parallel VF1 veins overprinted by VF3-STF2 bed-perpendicular vein-stylolite arrays indicating right-lateral shearing. The latter, in turn, are overprinted by VF4-STF3 bed-perpendicular vein-stylolite arrays indicating left-lateral shearing. Fault-parallel VF1 veins of both TF1 and TF2 faults are filled by multiple generations of calcite (Cal-1 to Cal-4). VF3 veins of both TF1 and TF2 faults are filled by Cal-1 cements. VF4 veins of TF1 are filled by Cal-2 to Cal-4 whereas those of TF2 faults by Cal-1 to Cal-4 cements (Figure 15b).

8. Discussion

8.1. Deformation Progression and Fold Evolution

Information summarized in Figure 15 allows us to propose a multistage tectonic evolution for the Parmelan anticline. The starting scenario includes development of Mesozoic to Early Tertiary NE-SW trending extensional fault systems (LF) dissecting Urgonian Limestones and Calcaires gréseux à miches (Figure 16a) and likely formed in the forebulge of the outer foreland basin system (DeCelles & Giles, 1996), where extensional stress fields typically occur (Allen et al., 1991; Billi & Salvini, 2003; Sinclair, 1997). The pre-folding activity of NE-trending extensional faults is confirmed in the study area by the evidence that, in the forelimb of the Parmelan anticline, synthetic subsidiary LF faults in the footwall of the major Enclave Fault have been passively rotated during folding (Figure 5i). Such a structural inheritance is well described in the northern Subalpine chains, where pre- to syn-orogenic NW-SE extension occurred in the Late Cretaceous/beginning of the Tertiary, on NE-trending extensional fault systems (Butler et al., 2018; Chaplet, 1992; Charollais et al., 1988; Gidon, 1998; Villars, 1986; Welbon, 1988; Welbon & Butler, 1992). In particular, according to Charollais et al. (1988), NE-trending high-angle faults formed in response to the overall uplift, emersion, and erosion of the Dauphinois margin (i.e., regional Paleocene unconformity). Syn-sedimentary fault activity indicates that some of the NE-trending extensional faults were already active in Early Late Cretaceous times (Gidon, 1998; Welbon, 1988). An Early Late Cretaceous extensional episode was documented also in the Chartreuse Massif (Gidon, 1992) and in the Vercors (Gidon, 1995). NE-striking Late Cretaceous extensional fault systems controlling deposition of Maastrichtian sediments were described also in the Wildhorn nappe of the Helvetic domain (Cardello & Mancktelow, 2014).

The evidence that some TF2 faults developed by linkage of V1 veins and that TF2 systematically abut TF1 faults, may suggest an incremental evolution from V1 to TF2 in the same deformation event. A major consequence of this inference is that TF1 and, possibly, VF1 veins, are older than V1 veins and ST1 stylolites. Despite such a loose chronological constraint does not allow proposing a robust solution for the formation of TF1 faults, their orientation perpendicular to LF faults might support development as fracture corridors and/or low-displacements release extensional faults (Destro, 1995) accommodating along strike stretching and transversal synclinal folding in the foredeep because of differential subsidence (Di Martire et al., 2015; Tavani, Storti et al., 2015; Figure 16a).

The older syn-orogenic background deformation structures are V1 calcite veins associated with ST1 stylolites (Figure 15a). The coincidence between V1 geometry in the crestal plateau of the Parmelan anticline and the unfolded attitudes obtained from the limbs (Figures 8, 10 and 12), indicates that V1 veins and ST1 stylolites formed before fold amplification, in a stress field with a horizontal maximum principal axis striking NNW-SSE, at high angle to the inherited LF fault zones (Figure 16b).

The onset of contraction likely caused buttressing on LF faults despite the latter were not perpendicular to the maximum compressional axis of the stress ellipsoid. Actually, the orientation of VF2 veins and STF1 stylolites indicates that deformation developed under a NW-SE compression i.e., strictly perpendicular to the fault trend (Figure 15a). Such orientation can likely represent a local stress field influenced by the proximity to the fault zones and it is not necessarily coincident with the far-field stress (Beaudoin et al., 2016; Homberg et al., 1997). This inference accounts for the absence of V1 veins in the damage zones of LF faults, suggesting that buttressing deformation started during early layer-parallel shortening and then continued in the following evolutionary stages. In the same stress regime, the orientation of TF1 extensional faults and fracture corridors caused their re-activation as right-lateral strike-slip fault zones. In this stress field, formation of TF2 faults might have started as dilational features propagating in the σ_1-σ_2 principal plane of the stress ellipsoid. Some right- and/or left-lateral strike-slip activity along TF2 fault zones might have been

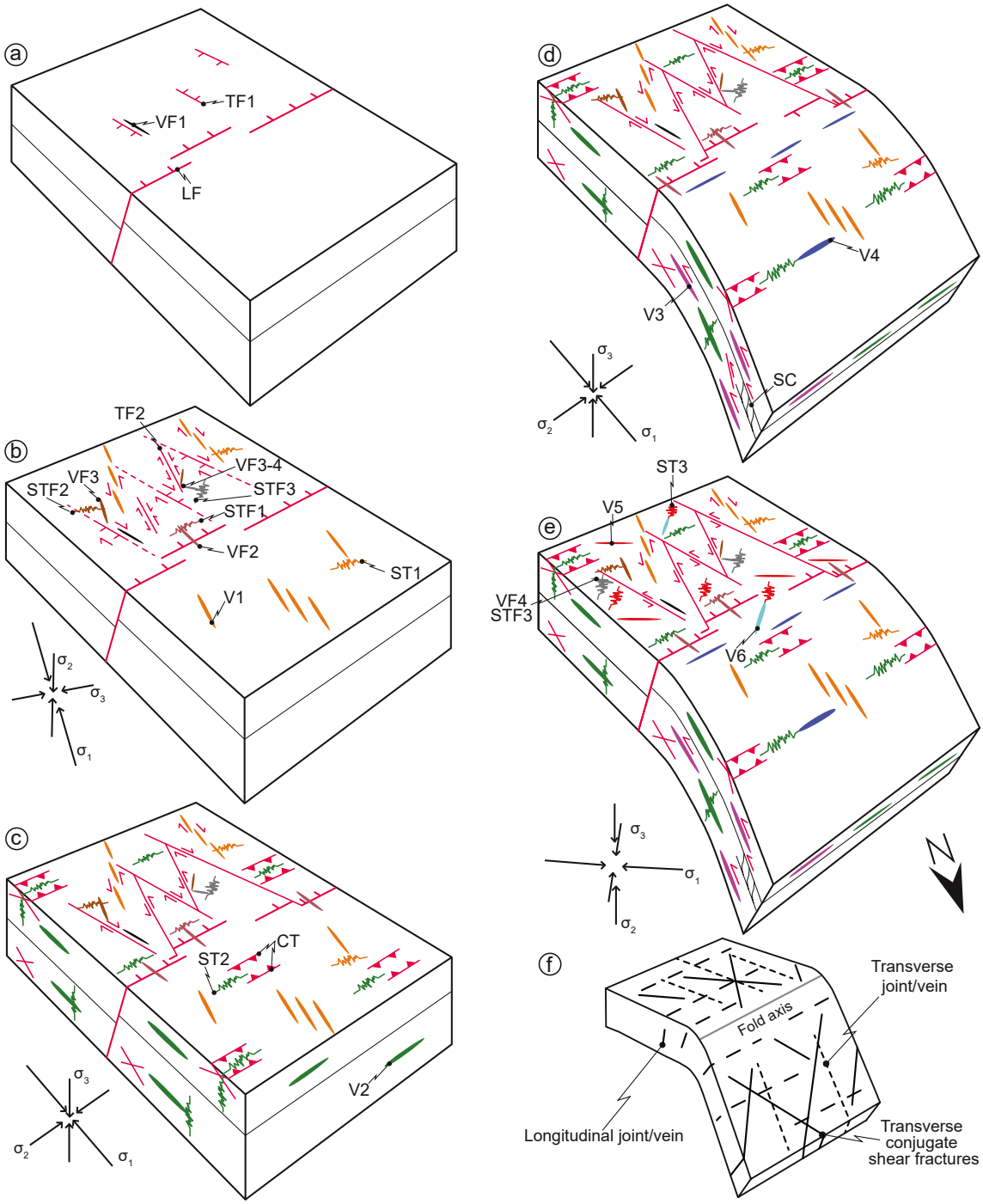

Figure 16. (a-e) Schematic sketches illustrating timing and kinematics of major faults, the evolution in space-and-time of the background deformation pattern, and the inferred stress fields. Colors of background and fault-related deformation structures are as given in previous figures. In each stage, only newly formed faults and deformation structures are labeled. (a) Pre-folding extension in the forebulge, (b) tectonic compaction preceding folding under a NNW-directed compression in a strike-slip stress configuration, (c) layer-parallel shortening under a NW-directed compression in a contractional stress configuration, (d) folding under a NW-directed compression in a contractional stress configuration, (e) post-folding oblique contraction (W-directed compression) in a strike-slip stress configuration during fold exhumation. In the sketches (a–e), the limb is representative of both forelimb and backlimb. (f) Conceptual model of fold-related deformation structures (after Cosgrove & Ameen, 2000).

induced by tear faulting or small amounts of clockwise block rotations during incipient dextral shearing along TF1 (Figure 16b).

Strong similarity between the orientation of unfolded CT thrust, ST2 stylolite, and V2 vein data from both fold limbs (Figures 8 and 12), and those exposed in the crestal plateau of the Parmelan anticline (Figure 10), and their kinematic congruency, indicate that this structural assemblage formed by layer-parallel shortening post-dating vertical compaction and preceding folding, in a contractional tectonic regime with a stress tensor displaying horizontal σ_1 striking NW-SE and vertical σ_3 (Figure 16c). During this stage, hinterland-dipping thrusts cutting through Cretaceous units possibly formed as attested by the Chevauchement de Pierre Taillée in the Parmelan forelimb that enabled the duplication of Urgonian Limestones (Figures 3a and 4b). The prosecution of buttressing eventually triggered folding of the carbonate multilayer (Figure 16d). Fold amplification by flexural-slip folding (e.g., Donath & Parker, 1964) produced S-C arrays indicating top-to-the crest shearing and associated V3 veins in fold limbs (Figures 9 and 12). Hinge-parallel V4 veins formed at this stage in the maximum curvature sectors of the Urgonian limestone, frequently by dilating ST2 stylolites, likely by tangential-longitudinal strain (e.g., Fischer & Wilkerson, 2000; Lemiszki et al., 1994; Ramsay, 1967). Localization of V4 veins in the hinge zones excludes extensive migration of rock volumes through axial surfaces and suggests that the Parmelan anticline developed by fixed hinge folding (e.g., Salvini & Storti, 2001), with progressive rotation of the limbs that maintained nearly constant lengths (e.g., Epard & Groshong, 1995; Fischer et al., 1992; Mitra, 2003).

The circular shapes of the Mont Téret, Ablon and Tête Ronde fold train, to the SE of the Parmelan anticline (Figure 2), and the presence of competent Cretaceous mechanical units overlapping incompetent ones (Figure 1c), support décollement folding as the dominant fold kinematics in the Bornes. The markedly different, box fold cross-sectional geometry of the Parmelan anticline, despite formed in the same mechanical stratigraphy, suggests that structural inheritance strongly influenced the first order fold geometry and kinematics (Butler et al., 2019; Gidon, 1996). In particular, the Enclave Fault System may have provided a mechanical weakness zone that, together with the thickness of the Urgonian Limestone competent mechanical unit (e.g., Casey & Butler, 2004; Currie et al., 1962; Fischer et al., 1992; Sepehr et al., 2006), fundamentally impacted on fold geometry and kinematics by behaving as a major sharp hinge zone that localized the crest-to-forelimb transition (e.g., Bazalgette et al., 2010) and promoted fixed-hinge folding.

Major thrusting and folding in the northern Subalpine chains occurred in Middle Miocene times (Bellahsen et al., 2014 and references therein), as indicated by Langhian-Serravallian syntectonic deformations in the Upper Marine Molasse (Beck et al., 1998). Burdigalian growth strata are preserved in the central molasse basin anticlines (Salève and Montagne d'Age), then affected by out-of-sequence thrusting along the Subalpine Thrust Front (Deville et al., 1994), which involves Aquitanian sediments in the footwall in the Semnoz area, SW of Annecy (Figure 1b; Huggenberger & Wildi, 1991). Accordingly, we propose a Lower Miocene age for the layer-parallel shortening and the start of the Parmelan anticline growth.

The association of V5 veins and ST3 stylolites, their overprinting relationships in the complex structural assemblage of the crestal plateau, and the oblique strike with respect to the fold axial trend (Figure 15a), indicate a new stress field characterized by an $\sim$ E-W maximum horizontal compressional axis σ_1 and a vertical σ_2 postdating the bulk growth of the Parmelan anticline (Figure 16e). During this post-folding stage, further re-activation of V1 veins occurred (Figures 11b). Local dilation of ST3 stylolites and formation of V6 veins is not compatible with E-W contraction. Moreover, E-W trending V5 veins are not affected by pressure solution and E-W stylolites associated with V6 veins were not observed, thus ruling out N-S compression at the fold-scale. A possible explanation for ST3 stylolite dilation is tangential longitudinal extension triggered by post-folding development of forelandward fold convexity in the Bornes, which is particularly accentuated in the southern sector of the massif.

8.2. Paleostress Analysis From Structural Data

Despite paleostress analysis was not the main purpose of our work, the large structural data set collected in the Parmelan anticline, including overprinting relationships among deformation structures, provides the opportunity to attempt paleostress reconstructions for the syn-orogenic geodynamic setting of this sector of the Alpine belt.

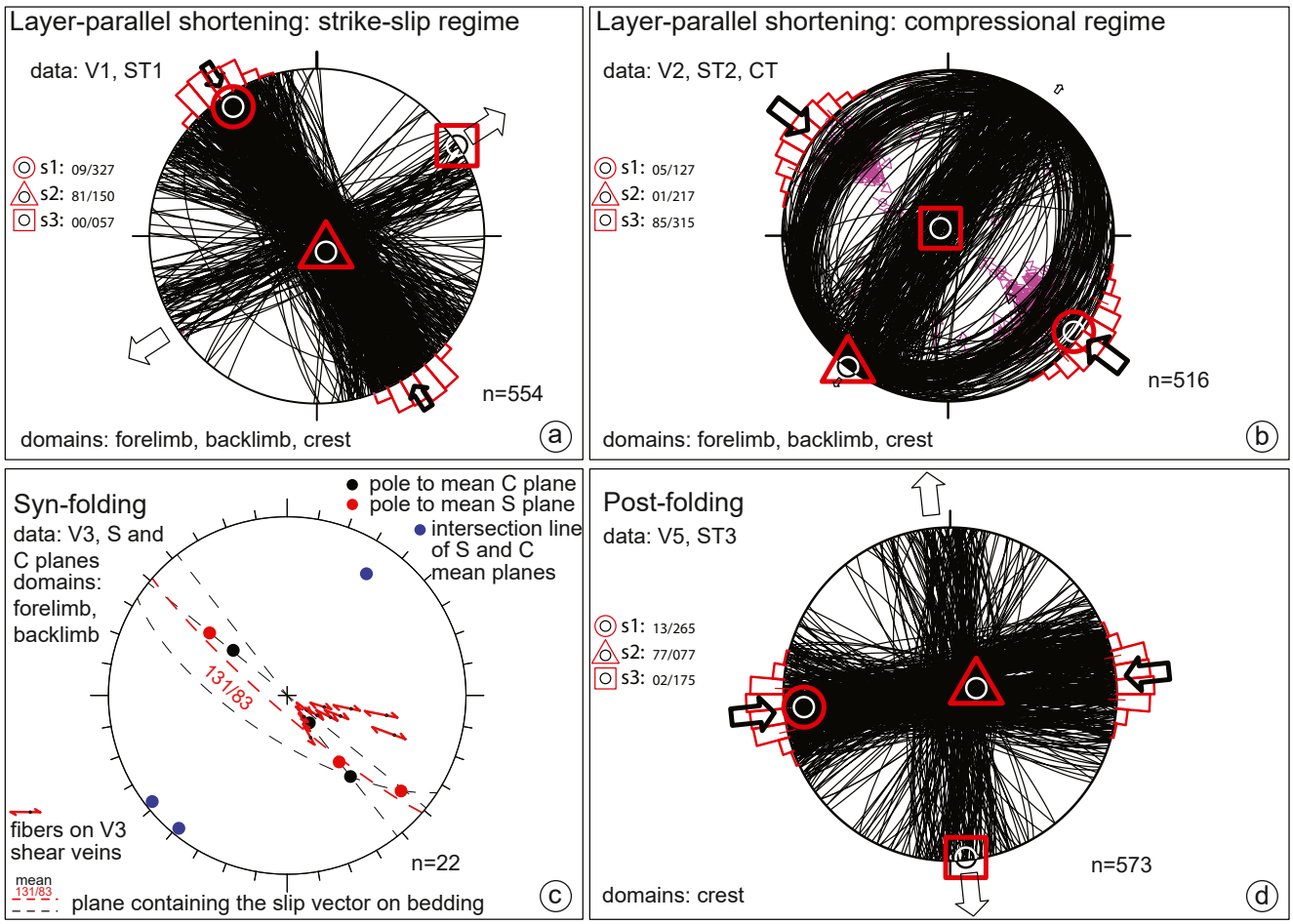

Figure 17. Stereographic projections showing merged data sets (data are from different structural domains within the anticline). Each stereographic projection shows a structurally compatible association of structures (mode I-II veins, stylolites and mesofaults) that formed under the same stress configuration. Each association of structures correspond to a particular stage in the evolution of the anticline: (a) pre-folding layer-parallel shortening in strike-slip regime, (b) pre-folding layer-parallel shortening in compressional regime, (c) syn-folding, (d) post-folding. The four associations were used to infer the orientations of principal stress axis and the results are shown in this figure.

Inversion of V1-ST1 data provides a stress tensor displaying a horizontal σ_1 striking N147°E and a vertical σ_2 (Figure 17a). Such a configuration of the principal stress axes indicates a strike-slip stress field (e.g., Hancock, 1985). Inversion of CT, V2 and ST2 data provides a stress tensor displaying a horizontal σ_1 striking N127°E and a vertical σ_3 (Figure 17b). This indicates that a permutation from vertical σ_2 to σ_3 occurred and that layer-parallel shortening resumed before the Parmelan anticline started to develop. Stress permutations to contractional regimes before folding have been documented in several cases and interpreted as the effect of the stress buildup during layer-parallel shortening (Amrouch et al., 2010, 2011; Ferrill et al., 2021; Tavani, Storti, et al., 2015). In the study area of the Bornes, the new stress field configuration was accompanied by a counterclockwise rotation of σ_1 by 20° with respect to the first event of layer-parallel shortening in the foreland basin system. The mean plane containing the slip vector on bedding planes (N131°E) obtained for the syn-folding stage from S-C fabrics, is compatible with slickenfibers on V3 flexural slip-related veins and agrees with the orientation of σ_1 provided by the inversion of cumulative contractional late layer-parallel shortening data (Figures 17b and 17c). This evidence indicates that the progression from late layer-parallel shortening to fold amplification occurred under the same overall stress field configuration and orientation.

Inversion of V5 vein and ST3 stylolite data provides a post-folding stress field configuration with a near horizontal principal axis σ_1 striking N85°E and a near vertical σ_2 (Figure 17d). This indicates that another permutation of the stress ellipsoid from vertical σ_3 to σ_2 occurred after the growth of the Parmelan anticline,

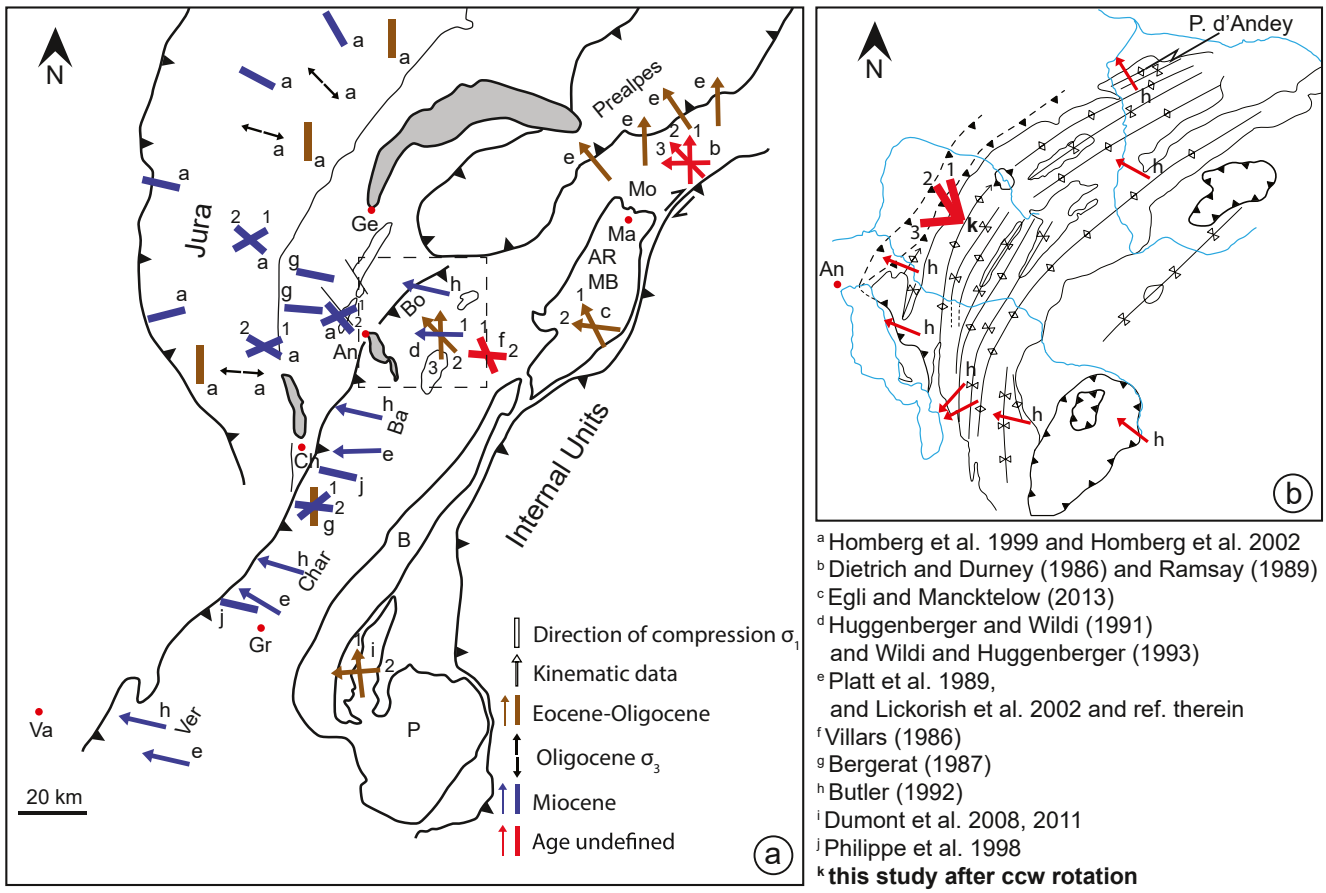

Figure 18. (a) Cenozoic stress field evolution in the External Western Alps. Va: Valence; Gr: Grenoble; Ch: Chambéry; An: Annecy; Ge: Genève; Ma: Martigny. P: Pelvoux; B: Belledonne; AR-MB: Aiguille Rouge-Mont Blanc; Ver: Vercors; Char: Chartreuse; Ba: Bauges; Bo: Bornes; Mo: Morcles. The dashed square indicates the area in b. (b) Simplified tectonic sketch map of the Bornes. In both a and b, numbers indicate relative chronology when more than one tectonic stage is documented.

with the onset of a new strike-slip stress field configuration. The switch between contractional and strike-slip stress regimes was accompanied by a counterclockwise rotation of σ_1 by about 42°.

Despite we are aware that using data from only a limited area of the Bornes Massif does not allow us to provide any robust contribution to significantly improve paleostress patterns and tectonic reconstructions at the regional scale, comparison with information available in the literature is in any case worth to be discussed, with the purpose of supporting future work on this subject. It is well known that syn-orogenic deformation in the Helvetic-Dauphinois domain is characterized by a polyphase tectonic evolution involving switches between different stress regimes and rotations of the maximum principal stress axis (Bergerat, 1985, 1987; Dietrich & Durney, 1986; Homberg et al., 1999, 2002; Huggenberger & Wildi, 1991; Laubscher, 1992; Philippe et al., 1998; Ramsay, 1989; Villars, 1986; Wildi & Huggenberger, 1993). Polyphase tectonic evolutions have been reported also from the external crystalline massifs (e.g., Dumont et al., 2008, 2011; Egli & Mancktelow, 2013; Figure 18a).

Care must be taken in the regional interpretation of the stress fields modeled from the two pre-folding layer-parallel shortening assemblages (Figures 17a and 17b) since they likely occurred before the formation of the Bornes salient presently testified by the along strike variable axial trend of the more external anticlines, which strike N62°E in the Pointe d'Andey sector and N41°E in the Parmelan plateau (Figures 1a and 3b), oroclinal bending that likely occurred during the syn- to post-folding stages (Ferrill & Groshong, 1993), possibly under the post-folding stress regime. If we assume that the anticlines initially had a linear NE-SW axial trend (Ferrill & Groshong, 1993), then a CCW rotation of 21° about a vertical axis can be inferred for the study area. By applying the same rotational angle to the σ_1–σ_2 principal plane of the stress ellipsoid

that produced V1 veins and ST1 stylolites (Figure 17a), an azimuth of 169°E is obtained. A first tectonic episode dominated by a NNW-SSE to NW-SE tectonic transport direction is proposed by Huggenberger and Wildi (1991) and Wildi and Huggenberger (1993) for the Bornes Massif, whereas maximum compression directions calculated from paleostress analysis in the Chartreuse and Vercors, to the SE, indicate a relatively uniform trend at about N105°E (Philippe et al., 1998; Figure 18a). Therefore, at the scale of the entire Subalpine chains, there is no robust evidence for such a NNW-SSE directed compression (Figure 18a). A Late Cretaceous-Early Eocene "Pyrenean phase" induced by a N-S compression largely identified in Provence (e.g., Lacombe & Jolivet, 2005), well documented in the Jura (e.g., Homberg et al., 2002) and in the entire European platform to the north of Western Alpine Molasse Basin (e.g., Bergerat, 1987) has been vaguely documented also in the southern Subalpine chains, particularly in the Vercors and western Chartreuse massif (Philippe, 1995; Philippe et al., 1998; Figure 18a). An Eocene N-S contraction has been documented also in the external crystalline massifs and in their cover (Figure 18a) and it has been interpreted as resulting from the initial northward motion of Adria, rather than being produced by the Pyrenean orogeny (Dumont et al., 2008, 2011). However, this phase is poorly documented in the northern Subalpine chains (Bornes and Aravis) where it remains poorly supported by kinematic data and with undefined chronological constraints. Consequently, considering also the σ_1 azimuthal trend obtained from our data that differs from the Eocene σ_1 proposed for the more external domains (e.g., Jura, Bergerat et al., 1987) we consider unlikely a possible connection between the oldest contractional deformation structures documented in the Parmelan anticline and the "Pyrenean phase." We suggest that the V1-ST1 assemblage may have formed during the onset of the Alpine compression in this sector certainly before folding and thrusting namely in pre-Burdigalian times, pre-dating growth folding in the Salève and Montagne d'Age (Deville et al., 1994). This interpretation is in accordance with the first tectonic phase proposed for the Bornes Massif by Wildi and Huggenberger (1993) for which they reported a shortening direction varying in trend from NNW-SSE to NW-SE.

Analysis of the along strike variable axial trend of the Parmelan anticline can be used also for tectonically framing the following Miocene tectonic evolution, including the second layer-parallel-shortening event and subsequent fold growth. By maintaining the assumption of an initially linear trend of the fold axis, striking ~62°E, perpendicular to the tectonic transport direction, the latter can be inferred at ~152°E. After a CCW rotation of ~25° of the Parmelan sector, the NW-SE trending pre-folding σ_1 and the syn-folding transport direction are in very good agreement with kinematic data obtained from the Pointe d'Andey anticline (N150°E, Butler, 1992; in Figure 18b) and with the inferred tectonic transport direction perpendicular to it. However, a specific paleomagnetic study and a structural investigation at a larger scale in the Bornes would be beneficial for better framing the early stages of Alpine compression in the regional context.

The Late Miocene westward tectonic transport reported in the Bornes (Huggenberger & Wildi, 1991; Ferrill & Groshong, 1993; Wildi & Huggenberger, 1993) and reported also in the Aravis Massif (Villars, 1986) and in the Helvetic realm (e.g., Dietrich & Durney, 1986; Ramsay, 1989) is confirmed by our data that also show one more switch from contractional to strike-slip stress field configuration during the post-folding stage in the Parmelan anticline (Figure 18a). The geodynamic setting responsible for this E-W contraction is still controversial between regional transpression along NE-trending dextral shear zones (Billant et al., 2015; Hubbard & Mancktelow, 1992; Ramsay, 1989) or more local processes associated with the final stages of oroclinal bending in the southern Bornes and with the activity of the Vuache Fault (Butler, 1992; Ferrill & Groshong, 1993). Tackling this open problem was not the purpose of our work in the Parmelan anticline and would need a different scale of investigation.

8.3. Impact of Structural Inheritance on Folding-Related Deformation

Folding-related deformation structure geometry typically includes both longitudinal and transversal features having classical angular relationships with fold axial trends (e.g., Cosgrove & Ameen, 2000; Price & Cosgrove, 1990; Stearns, 1968, Figure 16f). The syn-folding deformation pattern in the Parmelan anticline differs from such a template because transversal shear fractures are misoriented and tensile ones do not occur. Fold-perpendicular tensile deformation structures are typically documented in most anticlines worldwide (e.g., Awdal et al., 2016; Beaudoin et al., 2012, 2020; Bellahsen et al., 2006; Carminati et al., 2014; Casini et al., 2011; Evans et al., 2012; Guiton, Sassi, et al., 2003; Gutiérrez-Alonso & Gross, 1999; Hayes & Hanks, 2008; Silliphant et al., 2002; Storti & Salvini, 2001; Tavani et al., 2008; Tavani, Storti et al., 2015).

Inhibition of transversal jointing during growth of the Parmelan anticline may have been caused by the presence of inherited fractures (TF1 and VF1) striking perpendicular to the Enclave Fault trend, which formed as "release faults and fracture corridors" (e.g., Destro, 1995) during foredeep-parallel stretching, a common feature during foreland basin system evolution (e.g., Di Martire et al., 2015; Quintà & Tavani, 2012; Scisciani et al., 2001; Tavani, Storti, et al., 2015; Tavani, Vignaroli, et al., 2015). These deformation structures trending sub-perpendicular to the fold axis were reactivated during layer-parallel shortening and folding, thus preventing formation of new transversal fracturing.

The same mechanical reason can help explaining the asymmetrical orientation and abundance of transversal shear fractures with respect to the fold axial strike (Figure 6a). Conjugate sets of transversal shear fractures bisected by transversal tensile ones are textbook features of folding-related deformation patterns (Figure 16f) and are commonly documented in many anticlines worldwide (Amrouch et al., 2011; Awdal et al., 2016; Casini et al., 2011; Storti & Salvini, 2001; Tavani et al., 2006; Tavani, Storti, et al., 2011). In the Parmelan anticline, strike-slip reactivation of inherited TF1 extensional faults and fracture corridors likely prevented the formation of classical transversal conjugate strike-slip fault pairs, favoring the syn-folding development of TF2 as linkage fault splays between adjacent TF1 faults. Misoriented inherited transversal features affected by strike-slip re-activation have been described in other folds worldwide, including the Bóixols anticline in the Spanish Pyrenees (Tavani, Mencos, et al., 2011).

Longitudinal structural inheritance, other than controlling fold geometry and evolution, strongly influenced also the folding-related deformation pattern in the Parmelan anticline because it inhibited abundant development of longitudinal veins/fractures in well-defined deformation panels (Storti & Salvini, 1996; Tavani et al., 2006). This is evident in the crest-to-forelimb hinge sector, where newly formed longitudinal veins (V4) are scarce, likely because the pre-existing weak zone provided by the Enclave Fault prevented significant stress concentration and facilitated limb rotation. It follows that, despite the Parmelan anticline likely grew by fixed-hinge folding, the presence of longitudinal mechanical weakness zones caused major differences in the deformation pattern at the crest-to-forelimb transition compared to what expected from conceptual templates and numerical models (e.g., Liu et al., 2016; Salvini & Storti, 2001). It is worth noting that other field examples (Beaudoin et al., 2014; Casini et al., 2011) demonstrate that the presence of inherited pre-folding longitudinal joints/faults does not necessarily imply the absence of newly formed longitudinal tensile fractures during folding. Such a non-univocal behavior suggests that a key factor controlling the abundance of syn-folding longitudinal fracturing when structural inheritance also occurs can be fault displacement, which is expected to control damage zone widths (e.g., Balsamo et al., 2019; Martinelli et al., 2020; Mayolle et al., 2019) and, hence, the degree of weakness of inherited fault zones during folding.

The rounded hinge sector at the crest-to-backlimb transition of the Parmelan anticline, where significant faulting preceding folding was not recognized (Figure 2b), provides the opportunity for a comparative test on the role of structural inheritance. There, longitudinal veins (V4) occur but, despite intense curvature in very thick carbonate platform strata, they are not abundant, have decimetric lengths and millimetric apertures, and commonly formed by dilation of longitudinal ST2 stylolites (Figure 12a). Such a quite unexpected feature can be associated with a number of factors including: (a) strong layer compartmentalization caused by multiple reactivations of inherited TF transversal faults; (b) re-activation of deformation structures developed by layer-parallel shortening preceding folding, under both strike-slip and compressional stress field configurations (e.g., Fischer & Jackson, 1999; Hernández & Franzese, 2017); (c) relative position of the Urgonian Limestone with respect to the neutral surface of the multilayer undergoing folding (e.g., Frehner, 2011; Liu et al., 2016; Ramsay, 1967); (d) environmental conditions of deformation, namely regional strain rate, viscosity, permeability and, hence, pore fluid pressure (Eckert et al., 2014; Lemiszki et al., 1994; Liu et al., 2016). Since longitudinal veins are scarce at the forelimb-crest transition and are not abundant at the backlimb-crest transition where inherited faults were not recognized, we infer that the presence of pre-folding structural inheritance was not the only factor preventing syn-folding longitudinal fracturing in the Parmelan anticline and that the aforementioned factors necessarily played a role.

Speculations proposed in this section are based on the implicit assumption that deformation structures formed after layer-parallel shortening and before the V5-ST3 assemblage are associated with intrinsic fold evolution. Actually, the great structural complexity at depth (Figure 1d) regardless of the adopted structural interpretation, whether dominant disharmonic buckle folding (e.g., Muirhead et al., 2019) or blind

duplexing (e.g., Bellahsen et al., 2014), may imply that part of structural inheritance ubiquitous re-activations might have had an external origin, caused by underthrusting and duplexing that passively produced a type 1 gentle fold interference pattern (Ramsay, 1967) in the external Bornes (Figure 2c). Despite geometric and kinematic congruence of the syn-folding deformation pattern supports intrinsic solutions, external contributions during interference folding can not be ruled out.

Subsurface fluid circulation and accumulation, namely hydrocarbons, geothermal fluids, aquifers and, more recently, methane and hydrogen at seasonal storage sites and CO_2 sequestration, is strongly influenced by secondary porosity patterns. Accordingly, accurate predictions of fracture distributions in the subsurface are mandatory for effective economic and environmental development of reservoirs (Fonta et al., 2007; Roure et al., 2005). Despite early predictive templates of cross-sectional deformation patterns in undeformed layer-cake stratigraphy (Erickson & Jamison, 1995; Lemiszki et al., 1994; Salvini & Storti, 2001; Storti & Salvini, 1996; among others) improved subsurface fracture modeling, successful incorporation of the broad natural variability strongly benefits from the study of field analogs, in terms of processes and deformation structure attributes (e.g., Balsamo et al., 2019; Giuffrida et al., 2019; Gutmanis et al., 2018; La Bruna et al., 2020; Lavenu et al., 2013; Martinelli et al., 2020; Smeraglia et al., 2021; Stephenson et al., 2007), even in the era of supercomputing, big data, and artificial intelligence. The tectonic style of the Bornes Massif, characterized by cover sedimentary rocks deformed in buckle folds overlying a lower multilayer dominated by thrusts and thrust-related anticlines, is broadly comparable with what documented in other orogenic belts, including the central Appalachians (e.g., Evans et al., 2012), the Anti-Atlas of Morocco (e.g., Guiton, Sassi, et al., 2003; Helg et al., 2004; Ismat, 2008), and the Andean foothills (Jimenez et al., 2013). Accordingly, we expect that geological settings comparable to that of the Parmelan anticline can occur in foreland basin hydrocarbon provinces and/or storage sites worldwide. In this view, the quite peculiar deformation pattern that characterizes this fold and the evolutionary pathway that we inferred from structural evidence, can contribute to improve fracture distribution predictions in reservoirs involving structural inheritance in carbonate platform stratigraphy. A major implication of the control exerted by structural inheritance on transversal fractures is that their spatial distribution, abundance, and timing are independent from the contractional history and fold kinematics. In the Parmelan anticline, multiple re-activation of TF inherited transversal faults produced strong strike-slip-related deformation and compartmentalization in the flat-lying crest of the anticline (Figures 6 and 7). Such a feature is totally unexpected and, hence unpredictable, in a box anticline developed by fixed-hinge folding, where the flat-lying crestal sector should have mostly experienced tectonic uplift and negligible folding-related deformation (e.g., Salvini & Storti, 2001).

9. Conclusions

The NE-SW trending Parmelan anticline, located in the Bornes Massif, at the mountain front of the external Western Alps, provides outstanding exposures of folded carbonate platform Urgonian Limestones. Structural analysis of the deformation pattern recorded in this formation and in the underlying Calcaires gréseux à miches, combined with petrographical and geochemical analysis of vein-filling calcite cements, leads to the following major conclusive points.

1. The tectonic evolution of the region involved (i) extensional faulting, likely in the forebulge, including transversal release faulting and jointing; (ii) two events of layer-parallel shortening and buttressing of extensional structural inheritance preceding folding; (iii) growth of the Parmelan anticline; (iv) post-folding oblique contraction.
2. During evolutionary stages (ii) to (iv), the regional stress field underwent permutations of the vertical principal axis from σ_2 to σ_3, and then σ_2 again, in the late-stage evolution. Moreover, a progressive counterclockwise rotation of the horizontal maximum principal axis of the stress ellipsoid σ_1 accompanied σ_2–σ_3 switching, from a NNW-SSE azimuthal trend during stage (ii), to a NW-SE azimuth during stage (ii and iii), up to ~E-W in the final stage (iv).
3. The structural pattern exposed in the Parmelan anticline is strongly influenced by early syn-orogenic structural inheritance and pre-folding deformation structures. Longitudinal extensional faults underwent buttressing and localized the crest-forelimb transition, whereas transversal faults and vein corridors provided a structural framework that significantly constrained the progression of deformation during layer-parallel shortening preceding folding. The deformation assemblages produced by layer-parallel

shortening include bed-perpendicular and bed-parallel veins and associated stylolites, and conjugate subsidiary thrust faults.

4. Syn-folding deformations structures are not abundant, apart from widespread flexural-slip-related S-C shear fabric and bedding-parallel shear veins in the Calcaires gréseux à miches. In the Urgonian Limestones, only some subsidiary thrusts with a top-to-the anticlinal crest shear sense developed to facilitate layer-parallel slip. Moreover, a population of scarce hinge-parallel longitudinal veins developed in the crest-to-limb transitional domains, particularly in the backlimb-crest hinge sector.
5. A post-folding vein-stylolite association, both trending oblique to the Parmelan fold axial strike, developed in the crest of the anticline under a strike-slip stress field configuration and overprinted the pre-existing pre- and syn-folding deformation fabrics.

This work confirms the importance of pre-folding structural inheritance to determine fold kinematics and syn-folding deformation pattern development. Widespread abundance at convergent plate margins of pre-orogenic inherited extensional fault systems and of syn-orogenic incremental structural inheritance developed in foreland basin systems, implies that structural information collected in the Parmelan anticline is of general relevance for the comprehensive knowledge of evolutionary pathway templates in folds developed in foreland basin systems worldwide. The large data set and its sequential restoration in well-defined structural assemblages associated with specific evolutionary stages, can provide further support to predictive modeling of deformation patterns in subsurface reservoirs for hydrocarbons and geothermal fluid exploitation, methane and hydrogen seasonal storage, CO_2 sequestration, and aquifer management in fractured rocks. In this view, results from our work in the Parmelan anticline are of particular relevance because deformation patterns documented in the field are different from classical textbook templates.

Data Availability Statement

Data presented in this work can be found at: https://data.mendeley.com/datasets/hctvhs5b7d/1 (DOI: 10.17632/hctvhs5b7d.1).

Acknowledgments
This work is part of Luigi Berio's Ph.D. thesis, funded by Eni (SEFRAC Project; grants to A. Bistacchi and F. Storti). We gratefully acknowledge Eni for releasing this material for publication. We are grateful to A. Comelli for thin-section preparation and to E. Selmo for isotope analysis. The research has benefited from the equipment and framework of the COMP-HUB Initiative, funded by the 'Departments of Excellence' program of the Italian Ministry for Education, University and Research (MIUR, 2018–2022). The manuscript strongly benefitted from constructive criticism from two anonymous reviewers and Associate Editor, and from effective editorial handling by Laurent Jolivet. Luigi Berio wrote the manuscript and collect field and laboratory data; Fabrizio Storti wrote the manuscript and participated in the fieldwork; Fabrizio Balsamo, Silvia Mittempergher, Andrea Bistacchi and Marco Meda participated in the fieldwork and took part in data discussion and interpretation. Open Access Funding provided by Universita degli Studi di Parma within the CRUI-CARE Agreement.

References

Affolter, T., Faure, J. L., Gratier, J. P., & Colletta, B. (2008). Kinematic models of deformation at the front of the Alps: New data from map-view restoration. *Swiss Journal of Geosciences*, *101*(2), 289–303. https://doi.org/10.1007/s00015-008-1263-3

Allen, P. A., Crampton, S. L., & Sinclair, H. D. (1991). The inception and early evolution of the north Alpine foreland basin, Switzerland. *Basin Research*, *3*(3), 143–163. https://doi.org/10.1111/j.1365-2117.1991.tb00124.x

Amrouch, K., Beaudoin, N., Lacombe, O., Bellahsen, N., & Daniel, J. M. (2011). Paleostress magnitudes in folded sedimentary rocks. *Geophysical Research Letters*, *38*(17), 2. https://doi.org/10.1029/2011GL048649

Amrouch, K., Robion, P., Callot, J. P., Lacombe, O., Daniel, J. M., Bellahsen, N., & Faure, J. L. (2010). Constraints on deformation mechanisms during folding provided by rock physical properties: A case study at Sheep Mountain anticline (Wyoming, USA). *Geophysical Journal International*, *182*(3), 1105–1123. https://doi.org/10.1111/j.1365-246X.2010.04673.x

Awdal, A., Healy, D., & Alsop, G. I. (2016). Fracture patterns and petrophysical properties of carbonates undergoing regional folding: A case study from Kurdistan, N Iraq. *Marine and Petroleum Geology*, *71*, 149–167. https://doi.org/10.1016/j.marpetgeo.2015.12.017

Balsamo, F., Clemenzi, L., Storti, F., Solum, J., & Taberner, C. (2019). Tectonic control on vein attributes and deformation intensity in fault damage zones affecting Natih platform carbonates, Jabal Qusaybah, North Oman. *Journal of Structural Geology*, *122*(February), 38–57. https://doi.org/10.1016/j.jsg.2019.02.009

Bazalgette, L., Petit, J. P., Amrhar, M., & Ouanaïmi, H. (2010). Aspects and origins of fractured dip-domain boundaries in folded carbonate rocks. *Journal of Structural Geology*, *32*(4), 523–536. https://doi.org/10.1016/j.jsg.2010.03.002

Beaudoin, N., Koehn, D., Lacombe, O., Lecouty, A., Billi, A., Aharonov, E., & Parlangeau, C. (2016). Fingerprinting stress: Stylolite and calcite twinning paleopiezometry revealing the complexity of progressive stress patterns during folding—The case of the Monte Nero anticline in the Apennines, Italy. *Tectonics*, *35*, 1687–1712. https://doi.org/10.1002/2016TC004128.Received

Beaudoin, N., Labeur, A., Lacombe, O., Koehn, D., Billi, A., Hoareau, G., et al. (2020). Regional-scale paleofluid system across the Tuscan Nappe-Umbria-Marche Apennine Ridge (northern Apennines) as revealed by mesostructural and isotopic analyses of stylolite-vein networks. *Solid Earth*, *11*(4), 1617–1641. https://doi.org/10.5194/se-11-1617-2020

Beaudoin, N., Lacombe, O., Bellahsen, N., Amrouch, K., & Daniel, J. M. (2014). Evolution of pore-fluid pressure during folding and basin contraction in overpressured reservoirs: Insights from the Madison-Phosphoria carbonate formations in the Bighorn Basin (Wyoming, USA). *Marine and Petroleum Geology*, *55*, 214–229. https://doi.org/10.1016/j.marpetgeo.2013.12.009

Beaudoin, N., Leprêtre, R., Bellahsen, N., Lacombe, O., Amrouch, K., Callot, J. P., et al. (2012). Structural and microstructural evolution of the Rattlesnake Mountain Anticline (Wyoming, USA): New insights into the Sevier and Laramide orogenic stress build-up in the Bighorn Basin. *Tectonophysics*, *576–577*, 20–45. https://doi.org/10.1016/j.tecto.2012.03.036

Beck, C., Deville, E., Blanc, E., Philippe, Y., & Tardy, M. (1998). Horizontal shortening control of Middle Miocene marine siliciclastic accumulation (Upper Marine Molasse) in the southern termination of the Savoy Molasse Basin (northwestern Alps/southern Jura). *Geological Society, London, Special Publications*, *134*, 263–278. https://doi.org/10.1144/gsl.sp.1998.134.01.12

Bellahsen, N., Fiore, P., & Pollard, D. D. (2006). The role of fractures in the structural interpretation of Sheep Mountain Anticline, Wyoming. *Journal of Structural Geology*, *28*(5), 850–867. https://doi.org/10.1016/j.jsg.2006.01.013

Bellahsen, N., Mouthereau, F., Boutoux, A., Bellanger, M., Lacombe, O., Jolivet, L., & Rolland, Y. (2014). Collision kinematics in the Western external Alps. *Tectonics*, *33*(6), 1055–1088. https://doi.org/10.1002/2013TC003453
Bergbauer, S., & Pollard, D. D. (2004). A new conceptual fold-fracture model including prefolding joints, based on the Emigrant Gap anticline, Wyoming. *Bulletin of the Geological Society of America*, *116*(3–4), 294–307. https://doi.org/10.1130/B25225.1
Bergerat, F. (1985). Déformations cassantes et champs de contrainte tertiaires dans la plate-forme européenne, (Doctoral dissertation). Retrived from https://tel.archives-ouvertes.fr/tel-00502834. Université Pierre et Marie Curie.
Bergerat, F. (1987). Stress fields in the European platform at the time of Africa-Eurasia collision. *Tectonics*, *6*(2), 99–132. https://doi.org/10.1029/tc006i002p00099
Billant, J., Hippolyte, J. C., & Bellier, O. (2015). Tectonic and geomorphic analysis of the Belledonne border fault and its extensions, Western Alps. *Tectonophysics*, *659*, 31–52. https://doi.org/10.1016/j.tecto.2015.07.025
Billi, A., & Salvini, F. (2003). Development of systematic joints in response to flexure-related fibre stress in flexed foreland plates: The Apulian forebulge case history, Italy. *Journal of Geodynamics*, *36*(4), 523–536. https://doi.org/10.1016/S0264-3707(03)00086-3
Bons, P. D., Elburg, M. A., & Gomez-Rivas, E. (2012). A review of the formation of tectonic veins and their microstructures. *Journal of Structural Geology*, *43*, 33–62. https://doi.org/10.1016/j.jsg.2012.07.005
Branellec, M., Callot, J. P., Nivière, B., & Rigenbach, J. C. (2015). The fracture network, a proxy for mesoscale deformation: Constraints on layer parallel shortening history from the Malargüe fold and thrust belt, Argentina. *Tectonics*, *34*, 623–647. https://doi.org/10.1002/2014TC003738.Received
Burkhard, M., & Sommaruga, A. (1998). Evolution of the western Swiss Molasse basin: Structural relations with the Alps and the Jura belt. *Geological Society, London, Special Publications*, *134*, 279–298. https://doi.org/10.1144/GSL.SP.1998.134.01.13
Butler, R. W. H. (1989). The influence of pre-existing basin structure on thrust system evolution in the Western Alps. *Geological Society, London, Special Publications*, *44*(1), 105–122. https://doi.org/10.1144/GSL.SP.1989.044.01.07
Butler, R. W. H. (1991). Hydrocarbon maturation, migration and tectonic loading in the Western Alpine foreland thrust belt. *Geological Society, London, Special Publications*, *59*(1), 227–244. https://doi.org/10.1144/GSL.SP.1991.059.01.15
Butler, R. W. H. (1992). Thrusting patterns in the NW French subalpine chains. *Annales Tectonicae*, *6*(2), 150–172.
Butler, R. W. H., Bond, C. E., Cooper, M. A., & Watkins, H. (2018). Interpreting structural geometry in fold-thrust belts: Why style matters. *Journal of Structural Geology*, *114*(June), 251–273. https://doi.org/10.1016/j.jsg.2018.06.019
Butler, R. W. H., Bond, C. E., Cooper, M. A., & Watkins, H. (2019). Fold–thrust structures – Where have all the buckles gone? *Geological Society, London, Special Publications*, *487*, 21–44. https://doi.org/10.1144/sp487.7
Carannante, S., Argnani, A., Massa, M., D'Alema, E., Lovati, S., Moretti, M., et al. (2015). The May 20 (MW 6.1) and 29 (MW 6.0), 2012, Emilia (Po Plain, northern Italy) earthquakes: New seismotectonic implications from subsurface geology and high-quality hypocenter location. *Tectonophysics*, *655*, 107–123. https://doi.org/10.1016/j.tecto.2015.05.015
Cardello, G. L., & Mancktelow, N. S. (2014). Cretaceous syn-sedimentary faulting in the Wildhorn Nappe (SW Switzerland). *Swiss Journal of Geosciences*, *107*(2–3), 223–250. https://doi.org/10.1007/s00015-014-0166-8
Carminati, E., Aldega, L., Trippetta, F., Shaban, A., Narimani, H., & Sherkati, S. (2014). Journal of Asian Earth Sciences Control of folding and faulting on fracturing in the Zagros (Iran): The Kuh-e-Sarbalesh anticline. *Journal of Asian Earth Sciences*, *79*, 400–414. https://doi.org/10.1016/j.jseaes.2013.10.018
Casey, M., & Butler, R. W. H. (2004). Modelling approaches to understanding fold development: Implications for hydrocarbon reservoirs. *Marine and Petroleum Geology*, *21*(7), 933–946. https://doi.org/10.1016/j.marpetgeo.2004.01.010
Casini, G., Gillespie, P. A., Vergés, J., Romaire, I., Fernández, N., Casciello, E., et al. (2011). Sub-seismic fractures in foreland fold and thrust belts: Insight from the Lurestan Province , Zagros Mountains , Iran. *Petroleum Geoscience*, *17*(3), 263–282. https://doi.org/10.1144/1354-079310-043
Chaplet, M. (1992). Relations stratigraphiques et tectoniques entre nappe des Aravis et Bornes externes dans le synclinal de nappes de Thones (Massif subalpin des Bornes - Haute-Savoie - France). *Eclogae Geologicae Helvetiae*, *85*(1), 23–43.
Charollais, J., Busnardo, R., Cardin, M., Clavel, B., Decrouez, D., Delamette, M., et al. (1988). *Notice explicative de la feuille Annecy-Bonneville à 1/50 000*. Editions Du BRGM. https://doi.org/10.2105/AJPH.2014.302260
Charollais, J., & Jamet, M. (1990). Principaux résultats géologiques du forage Brizon 1 (BZN 1) Haute-Savoie, France. *Mémoires de La Société Géologique de France*, *156*, 185–202.
Charollais, J., & Liermier, M. (1967). Sur la découverte d'une "fenêtre" dans le massif des Bornes (Haute-Savoie, France). *Compte rendu des séances de la Société de physique et d'histoire naturelle de Genève*, *2*(1), 107.
Charollais, J., Pairis, J.-L., & Rosset, J. (1977). Compte rendu de l'excursion de la Société Géologique Suisse en Haute-Savoie (France) du 10 au 12 Octobre 1976. *Eclogae Geologicae Helvetiae*, *70*, 253–285.
Clavel, B., Conrad, M. A., Busnardo, R., Charollais, J., & Granier, B. (2013). Mapping the rise and demise of Urgonian platforms (Late Hauterivian - Early Aptian) in southeastern France and the Swiss Jura. *Cretaceous Research*, *39*(February), 29–46. https://doi.org/10.1016/j.cretres.2012.02.009
Cosgrove, J. W., & Ameen, M. S. (2000). A comparison of the geometry, spatial organization and fracture patterns associated with forced folds and buckle folds. *Geological Society, London, Special Publications*, *169*, 7–21. https://doi.org/10.1144/GSL.SP.2000.169.01.02
Currie, J. B., Patnode, H. W., & Trump, R. P. (1962). Development of folds in sedimentary strata: [DOFISS]2.0. *Bulletin of the Geological Society of America*, *73*(6), 6552–673. https://doi.org/10.1130/0016-7606(1962)73[655:dofiss]2.0.co;2
Dal Piaz, V., Bistacchi, A., & Massironi, M. (2003). Geological outline of the Alps. *Geological outline of the Alps*, *26*(3), 175–180. https://doi.org/10.18814/epiiugs/2003/v26i3/004
DeCelles, P. G., & Giles, K. A. (1996). Foreland basin systems. *Basin Research*, *8*(2), 105–123. https://doi.org/10.1046/j.1365-2117.1996.01491.x
de Graciansky, P. C., Dardeau, G., Lemoine, M., & Tricart, P. (1989). The inverted margin of the French Alps and foreland basin inversion. *Geological Society, London, Special Publications*, *44*(1), 87–104. https://doi.org/10.1144/GSL.SP.1989.044.01.06
Delvaux, D., & Sperner, B. (2003). New aspects of tectonic stress inversion with reference to the TENSOR program. *Geological Society, London, Special Publications*, *212*, 75–100. https://doi.org/10.1144/GSL.SP.2003.212.01.06
Destro, N. (1995). Release fault: A variety of cross fault in linked extensional fault systems, in the Sergipe-Alagoas Basin, NE Brazil. *Journal of Structural Geology*, *17*(5), 615–629. https://doi.org/10.1016/0191-8141(94)00088-H
Deville, E., Blanc, E., Tardy, M., Beck, C., Cousin, M., & Ménard, G. (1994). Thrust propagation and syntectonic sedimentation in the Savoy Tertiary Molasse Basin (Alpine foreland). *Hydrocarbon and Petroleum Geology of France*, 269–280. https://doi.org/10.1007/978-3-642-78849-9_19
Deville, E., & Sassi, W. (2006). Contrasting thermal evolution of thrust systems: An analytical and modeling approach in the front of the western Alps. *AAPG Bulletin*, *90*(6), 887–907. https://doi.org/10.1306/01090605046

Dietrich, D., & Durney, D. W. (1986). Change of direction of overthrust shear in the Helvetic nappes of western Switzerland. *Journal of Structural Geology*, *8*(3–4), 389–398.
Di Martire, D., Ascione, A., Calcaterra, D., Pappalardo, G., & Mazzoli, S. (2015). Quaternary deformation in SE Sicily: Insights into the life and cycles of forebulge fault systems. *Lithosphere*, *7*(5), 519–534. https://doi.org/10.1130/L453.1
Donath, F. A., & Parker, R. B. (1964). Folds and Folding. *Geological Society of America Bulletin*, *75*, 45–62. https://doi.org/10.1130/0016-7606(1964)75[45:faf]2.0.co;2
Doudoux, B., Barféty, J. C., Carfantan, J. C., Tardy, M., & Nicoud, G. (1992). *Notice explicative, Carte géol. France (1/50 000), feuille Annecy—Ugine (702)) — Orléans*. BRGM.
Doudoux, B., Mercier, B., & Tardy, M. (1982). Une interpretation nouvelle de la structure des massifs subalpins savoyards (Alpes occldentales) nappes de charrriage oligocénes et déformations superposées. *Comptes Rendus de l'Académie des Sciences*. https://doi.org/10.1017/CBO9781107415324.004
Dumont, T., Champagnac, J. D., Crouzet, C., & Rochat, P. (2008). Multistage shortening in the Dauphiné zone (French Alps): The record of Alpine collision and implications for pre-Alpine restoration. *Swiss Journal of Geosciences*, *101*(SUPPL. 1), 89–110. https://doi.org/10.1007/s00015-008-1280-2
Dumont, T., Simon-Labric, T., Authemayou, C., & Heymes, T. (2011). Lateral termination of the north-directed Alpine orogeny and onset of westward escape in the Western Alpine arc: Structural and sedimentary evidence from the external zone. *Tectonics*, *30*(5), 1. https://doi.org/10.1029/2010TC002836
Eckert, A., Connolly, P., & Liu, X. (2014). Large-scale mechanical buckle fold development and the initiation of tensile fractures. *Geochemistry, Geophysics, Geosystems*, *15*, 4570–4587. https://doi.org/10.1002/2014GC00550210.1002/2014gc005502
Egli, D., & Mancktelow, N. (2013). The structural history of the Mont Blanc massif with regard to models for its recent exhumation. *Swiss Journal of Geosciences*, *106*(3), 469–489. https://doi.org/10.1007/s00015-013-0153-5
Epard, J. L. (1990). *La nappe de Morcles au sud-ouest du Mont-Blanc, (Doctoral dissertation)*. Université de Lausanne. Retrieved from https://tel.archives-ouvertes.fr/tel-00923347
Epard, J. L., & Groshong, R. H. (1995). Kinematic model of detachment folding including limb rotation, fixed hinges and layer-parallel strain. *Tectonophysics*, *247*, 85–103. https://doi.org/10.1016/0040-1951(94)00266-C
Erickson, S. G., & Jamison, W. R. (1995). Viscous-plastic finite-element models of fault-bend folds. *Journal of Structural Geology*, *17*(4), 561–573. https://doi.org/10.1016/0191-8141(94)00082-B
Evans, M. A., Bebout, G. E., & Brown, C. H. (2012). Changing fluid conditions during folding: An example from the central Appalachians. *Tectonophysics*, *576–577*, 99–115. https://doi.org/10.1016/j.tecto.2012.03.002
Ferket, H., Swennen, R., Ortuno, S., & Roure, F. (2003). Reconstruction of the fluid flow history during Laramide foreland fold and thrust belt development in eastern Mexico: Cathodoluminescence and 618O-613C isotope trends of calcite-cemented fractures. *Journal of Geochemical Exploration*, *6742*(03). https://doi.org/10.1016/S0375-6742
Ferrill, D. A., & Groshong, R. H. (1993). Kinematic model for the curvature of the northern Subalpine Chain, France. *Journal of Structural Geology*, *15*(3–5), 523–541. https://doi.org/10.1016/0191-8141(93)90146-2
Ferrill, D. A., Smart, K. J., Cawood, A. J., & Morris, A. P. (2021). The fold-thrust belt stress cycle : Superposition of normal , strike-slip , and thrust faulting deformation regimes. *Journal of Structural Geology*, *148*(May), 104362. https://doi.org/10.1016/j.jsg.2021.104362
Fischer, M. P., Higuera-Díaz, I. C., Evans, M. A., Perry, E. C., & Lefticariu, L. (2009). Fracture-controlled paleohydrology in a map-scale detachment fold: Insights from the analysis of fluid inclusions in calcite and quartz veins. *Journal of Structural Geology*, *31*(12), 1490–1510. https://doi.org/10.1016/j.jsg.2009.09.004
Fischer, M. P., & Jackson, P. B. (1999). Stratigraphic controls on deformation patterns in fault-related folds: A detachment fold example from the Sierra Madre Oriental, northeast Mexico. *Journal of Structural Geology*, *21*(6), 613–633. https://doi.org/10.1016/S0191-8141(99)00044-9
Fischer, M. P., & Wilkerson, M. S. (2000). Predicting the orientation of joints from fold shape: Results of pseudo-three-dimensional modeling and curvature analysis. *Geology*, *28*(1), 15–18. https://doi.org/10.1130/0091-7613(2000)028<0015:ptoojf>2.3.co;2
Fischer, M. P., Woodward, N. B., & Mitchell, M. M. (1992). The kinematics of break-thrust folds. *Journal of Structural Geology*, *14*(4), 451–460. https://doi.org/10.1016/0191-8141(92)90105-6
Fonta, O., Al-ajmi, H., Verma, N. K., Matar, S., Divry, V., & Al-Qallaf, H. (2007). *The fracture characterization and fracture modeling of a tight carbonate reservoir — the Najmah-Sargelu of West Kuwait* (pp. 12–15). SPE Reservoir Evaluation and Engineering.
Frehner, M. (2011). The neutral lines in buckle folds. *Journal of Structural Geology*, *33*(10), 1501–1508. https://doi.org/10.1016/j.jsg.2011.07.005
Gidon, M. (1992). Présence De Failles Synsédimentaires Aptiennes En Chartreuse (Alpes Occidentales, France). *Geologie Alpine*, *68*, 57–62. Retrieved from http://geologie-alpine.ujf-grenoble.fr/articles/GA_1992__68__57_0.pdf
Gidon, M. (1995). Une faille d'extension antérieure au plissement, sur le rebord oriental du Vercors. *Geologie Alpine*, *71*, 193–198. Retrieved from http://docu.gidon.free.fr/Z-art/GA_1995__71__193_0_fai-ext-Vercors.pdf
Gidon, M. (1996). Vues nouvelles sur la structure des massifs des Bornes et des Bauges orientales. *Geologie Alpine*, *72*, 35–59. Retrieved from http://geologie-alpine.ujf-grenoble.fr/articles/GA_1996__72__35_0.pdf
Gidon, M. (1998). Failles extensives antérieures au plissement dans les massifs subalpins: Un exemple nouveau dans le massif des Bornes (France). *Geologie Alpine*, *74*, 91–96. Retrieved from http://www.geol-alp.com/z_publications/98ga_arclosan.html
Giuffrida, A., La Bruna, V., Castelluccio, P., Panza, E., Rustichelli, A., Tondi, E., et al. (2019). Fracture simulation parameters of fractured reservoirs: Analogy with outcropping carbonates of the Inner Apulian Platform, southern Italy. *Journal of Structural Geology*, *123*(February), 18–41. https://doi.org/10.1016/j.jsg.2019.02.007
Guellec, S., Mugnier, J.-L., Tardy, M., & Roure, F. (1990). Neogene evolution of the western Alpine foreland in the light of ECORS data and balanced cross-section. *Deep structure of the Alps*, *156*, 165–184. Retrieved from http://cat.inist.fr/?aModele=afficheN&cpsidt=4341857
Guiton, M. L. E., Leroy, Y. M., & Sassi, W. (2003a). Activation of diffuse discontinuities and folding of sedimentary layers. *Journal of Geophysical Research*, *108*(B4), 2183. https://doi.org/10.1029/2002JB001770
Guiton, M. L. E., Sassi, W., Leroy, Y. M., & Gauthier, B. D. M. (2003b). Mechanical constraints on the chronology of fracture activation in folded Devonian sandstone of the western Moroccan Anti-Atlas. *Journal of Structural Geology*, *25*, 1317–1330. https://doi.org/10.1016/s0191-8141(02)00155-4
Gutiérrez-Alonso, G., & Gross, M. R. (1999). Structures and mechanisms associated with development of a fold in the Cantabrian zone thrust belt, NW Spain. *Journal of Structural Geology*, *21*(6), 653–670. https://doi.org/10.1016/S0191-8141(99)00055-3

Gutmanis, J., i Oró, L. A., Díez-Canseco, D., Chebbihi, L., Awdal, A., & Cook, A. (2018). Fracture analysis of outcrop analogues to support modelling of the subseismic domain in carbonate reservoirs, south-central Pyrenees. *Geological Society, London, Special Publications*, *459*(1), 139–156. https://doi.org/10.1144/sp459.2

Hancock, P. L. (1985). Brittle microtectonics: Principles and practice. *Journal of Structural Geology*, *7*(3–4), 437–457. https://doi.org/10.1016/0191-8141(85)90048-3

Hayes, M., & Hanks, C. L. (2008). Evolving mechanical stratigraphy during detachment folding. *Journal of Structural Geology*, *30*, 548–564. https://doi.org/10.1016/j.jsg.2008.01.006

Helg, U., Burkhard, M., Caritg, S., & Robert-Charrue, C. (2004). Folding and inversion tectonics in the Anti-Atlas of Morocco. *Tectonics*, *23*(4). https://doi.org/10.1029/2003TC001576

Hennings, P. H., Olson, J. E., & Thompson, L. B. (2000). Combining outcrop data and three-dimensional structural models to characterize fractured reservoirs: An example from Wyoming. *AAPG Bulletin*, *84*(6), 830–849. https://doi.org/10.1306/A967340A-1738-11D7-8645000102C1865D

Hernández, M., & Franzese, J. R. (2017). The fracture patterns of the Tin Tin anticline: Fracturing process during the foreland evolution in the Calchaquí Valley, northwestern Argentina. *Journal of Structural Geology*, *96*, 54–64. https://doi.org/10.1016/j.jsg.2017.01.011

Homberg, C., Bergerat, F., Philippe, Y., Lacombe, O., & Angelier, J. (2002). Structural inheritance and cenozoic stress fields in the Jura fold-and-thrust belt (France). *Tectonophysics*, *357*(1–4), 137–158. https://doi.org/10.1016/S0040-1951(02)00366-9

Homberg, C., Hu, J. C., Angelier, J., Bergerat, F., & Lacombe, O. (1997). Characterization of stress perturbations near major fault zones: Insights from 2-D distinct-element numerical modelling and field studies (Jura mountains). *Journal of Structural Geology*, *19*(5), 703–718. https://doi.org/10.1016/S0191-8141(96)00104-6

Homberg, C., Lacombe, O., Angelier, J., & Bergerat, F. (1999). New constraints for indentation mechanisms in arcuate belts from the Jura Mountains, France. *Geology*, *27*(9), 827–830. https://doi.org/10.1130/0091-7613(1999)02710.1130/0091-7613(1999)027<0827:ncfimi>2.3.co;2

Hubbard, M., & Mancktelow, N. S. (1992). Lateral displacement during Neogene convergence in the western and central Alps. *Geology*, *20*(10), 943–946. https://doi.org/10.1130/0091-7613(1992)020<0943:lddnci>2.3.co;2

Huggenberger, P., & Wildi, W. (1991). La tectonique du massif des Bornes (Chaînes Subalpines, Haute-Savoie, France). *Eclogae Geologicae Helvetiae*, *84*(1), 125–149.

Ismat, Z. (2008). Folding kinematics expressed in fracture patterns: An example from the Anti-Atlas fold belt, Morocco. *Journal of Structural Geology*, *30*(11), 1396–1404. https://doi.org/10.1016/j.jsg.2008.07.010

Jimenez, L., Mora, A., Casallas, W., Silva, A., Tesón, E., Tamara, J., et al. (2013). Segmentation and growth of foothill thrust-belts adjacent to inverted grabens: The case of the Colombian Llanos foothills. *Geological Society - Special Publications*, *377*(1), 149–154. https://doi.org/10.1144/sp377.11

La Bruna, V., Lamarche, J., Agosta, F., Rustichelli, A., Giuffrida, A., Salardon, R., & Mari, L. (2020). Structural diagenesis of shallow platform carbonates: Role of early embrittlement on fracture setting and distribution, case study of Monte Alpi (Southern Apennines, Italy). *Journal of Structural Geology*, *131*, 103940. https://doi.org/10.1016/j.jsg.2019.103940

Lacombe, O., Bellahsen, N., & Mouthereau, F. (2011). Fracture patterns in the Zagros Simply Folded Belt (Fars, Iran): Constraints on early collisional tectonic history and role of basement faults. *Geological Magazine*, *148*, 940–963. https://doi.org/10.1017/S001675681100029X

Lacombe, O., & Jolivet, L. (2005). Structural and kinematic relationships between Corsica and the Pyrenees-Provence domain at the time of the Pyrenean orogeny. *Tectonics*, *24*(1), 1. https://doi.org/10.1029/2004TC001673

Lateltin, O. (1988). *Les dépôts turbiditiques oligocènes d'avant-pays entre Annecy (Haute-Savoie) et le Sanetsch (Suisse): Grès de Taveyannaz et du Val d'Illiez, (doctoral dissertation)*. University of Fribourg.

Laubscher, H. P. (1977). Fold development in the Jura. *Tectonophysics*, *37*, 337–362. https://doi.org/10.1016/0040-1951(77)90056-7

Laubscher, H. P. (1992). Jura kinematics and the Molasse Basin. *Eclogae Geologicae Helvetiae*, *85*(3), 653–675.

Lavenu, A. P. C., Lamarche, J., Gallois, A., & Gauthier, B. D. M. (2013). Tectonic versus diagenetic origin of fractures in a naturally fractured carbonate reservoir analog (Nerthe anticline, southeastern France). *AAPG Bulletin*, *97*(12), 2207–2232. https://doi.org/10.1306/04041312225

Lefticariu, L., Perry, E. C., Fischer, M. P., & Banner, J. L. (2005). Evolution of fluid compartmentalization in a detachment fold complex. *Geology*, *33*(1), 69–72. https://doi.org/10.1130/G20592.1

Lemiszki, P. J., Landes, J. D., & Hatcher, R. D. (1994). Controls on hinge-parallel extension fracturing in single-layer tangential-longitudinal strain folds. *Journal of Geophysical Research*, *99*, 22027–22041. https://doi.org/10.1029/94jb01853

Lemoine, M., Bas, T., Arnaud-Vanneau, A., Arnaud, H., Dumont, T., Gidon, M., et al. (1986). The continental margin of the Mesozoic Tethys in the Western Alps. *Marine and Petroleum Geology*, *3*(3), 179–199. https://doi.org/10.1016/0264-8172(86)90044-9

Letouzey, J. (1990). Fault reactivation, inversion and fold-thrust belt. In J. Letouzey (Ed.), *Petroleum and tectonics in mobile belts* (pp. 101–128). Editions Technip.

Lickorish, W. H., Ford, M., Bürgisser, J., & Cobbold, P. R. (2002). Arcuate thrust systems in sandbox experiments: A comparison to the external arcs of the Western Alps. *Bulletin of the Geological Society of America*, *114*(9), 1089–1107. https://doi.org/10.1130/0016-7606(2002)114<1089:ATSISE>2.0.CO;2

Liu, X., Eckert, A., & Connolly, P. (2016). Stress evolution during 3D single-layer visco-elastic buckle folding: Implications for the initiation of fractures. *Tectonophysics*, *679*, 140–155. https://doi.org/10.1016/j.tecto.2016.04.042

Martinelli, M., Bistacchi, A., Mittempergher, S., Bonneau, F., Balsamo, F., Caumon, G., & Meda, M. (2020). Damage zone characterization combining scan-line and scan-area analysis on a km-scale Digital Outcrop Model: The Qala Fault (Gozo). *Journal of Structural Geology*, *140*(July), 104144. https://doi.org/10.1016/j.jsg.2020.104144

Martinez, M. C. (1976). *Contribution a l'etude geologique du sud-ouest du massif des Bornes entre la vallee du Fier et le lac d'Annecy , region de Bluffy et de Montremont, Haute-Savoie. (Doctoral dissertation)*. Université Pierre et Marie Curie. Retrieved from https://tel.archives-ouvertes.fr/tel-00743927

Mayolle, S., Soliva, R., Caniven, Y., Wibberley, C., Ballas, G., Milesi, G., & Dominguez, S. (2019). Scaling of fault damage zones in carbonate rocks. *Journal of Structural Geology*, *124*, 35–50. https://doi.org/10.1016/j.jsg.2019.03.007

Menkveld-Gfeller, U., Kempf, O., & Funk, H. (2016). Lithostratigraphic units of the Helvetic Palaeogene: Review, new definition, new classification. *Swiss Journal of Geosciences*, *109*(2), 171–199. https://doi.org/10.1007/s00015-016-0217-4

Mitra, S. (2003). A unified kinematic model for the evolution of detachment folds. *Journal of Structural Geology*, *25*(10), 1659–1673. https://doi.org/10.1016/S0191-8141(02)00198-0

Moss, S. (1992). *Burial diagenesis, organic maturation and tectonic loading in the French Subalpine Chains. (Doctoral dissertation)*. Durham University. Retrieved from http://etheses.dur.ac.uk/5865/

Moss, S., & Tucker, M. E. (1995). Diagenesis of Barremian-Aptian platform carbonates (the Urgonian Limestone Formation of SE France): Near-surface and shallow-burial diagenesis. *Sedimentology*, *42*(6), 853–874. https://doi.org/10.1111/j.1365-3091.1995.tb00414.x

Mugnier, J. L., Bergerat, F., Damotte, B., Guellec, S., Nicolas, A., Polino, R., et al. (1996). Crustal structure of the western Alps and their forelands. *Bulletin de la Société Géologique de France*, *170*, 73–97. Retrieved from http://cat.inist.fr/?aModele=afficheN&cpsidt=4341857

Muirhead, D. K., Bond, C. E., Watkins, H., Butler, R. W. H., Schito, A., Crawford, Z., & Marpino, A. (2019). Raman spectroscopy: An effective thermal marker in low temperature carbonaceous fold–thrust belts. *Geological Society, London, Special Publications*, *490*(1), 135–151. https://doi.org/10.1144/sp490-2019-27

Muñoz, J. A., Beamud, E., Fernández, O., Arbués, P., Dinarès-Turell, J., & Poblet, J. (2013). The Ainsa Fold and thrust oblique zone of the central Pyrenees: Kinematics of a curved contractional system from paleomagnetic and structural data. *Tectonics*, *32*(5), 1142–1175. https://doi.org/10.1002/tect.20070

Philippe, Y. (1995). *Rampes latérales et zones de transfert dans les chaînes plissées: Géométrie, conditions de formation et pièges structuraux associés. (Doctoral dissertation)*. Retrieved from https://tel.archives-ouvertes.fr/tel-00755680. Université de Savoie.

Philippe, Y., Deville, E., & Mascle, A. (1998). Thin-skinned inversion tectonics at oblique basin margins: Example of the western Vercors and Chartreuse Subalpine massifs (SE France). *Geological Society, London, Special Publications*, *134*(1), 239–262. https://doi.org/10.1144/GSL.SP.1998.134.01.11

Platt, J., Behrmann, J. H., Cunningham, J. F., Helman, M., Parish, M., Shepley, M. G., et al. (1989). Kinematics of the Alpine arc and the motion history of Adria. *Nature*, *337*(12), 158–161. https://doi.org/10.1038/337158a0

Price, N. J., & Cosgrove, J. W. (1990). *Analysis of geological structures* (p. 502). Cambridge University Press.

Quintà, A., & Tavani, S. (2012). The foreland deformation in the south-western Basque-Cantabrian Belt (Spain). *Tectonophysics*, *576–577*, 4–19. https://doi.org/10.1016/j.tecto.2012.02.015

Ramsay, J. G. (1967). *Folding and fracturing of rocks* (p. 568). McGraw-Hill Book Co.

Ramsay, J. G. (1989). Fold and fault geometry in the western Helvetic nappes of Switzerland and France and its implication for the evolution of the arc of the western Alps. *Geological Society, London, Special Publications*, *45*(1), 33–45. https://doi.org/10.1144/GSL.SP.1989.045.01.02

Roure, F., Swennen, R., Schneider, F., Faure, J. L., Ferket, H., Guilhaumou, N., et al. (2005). Incidence and importance of tectonics and natural fluid migration on reservoir evolution in foreland fold-and-thrust belts. *Oil and Gas Science and Technology*, *60*(1), 67–106. https://doi.org/10.2516/ogst:2005006

Salvini, F. (2019), *Daisy3, the Structural Data Integrated System Analyzer, Software, version 5.38*. Retrieved from https://host.uniroma3.it/progetti/fralab/Downloads/Daisy_Program/

Salvini, F., & Storti, F. (2001). The distribution of deformation in parallel fault-related folds with migrating axial surfaces: Comparison between fault-propagation and fault-bend folding. *Journal of Structural Geology*, *23*(1), 25–32. https://doi.org/10.1016/S0191-8141(00)00081-X

Sassi, W., Guiton, M. L. E., Leroy, Y. M., Daniel, J., & Callot, J. (2012). Constraints on bed scale fracture chronology with a FEM mechanical model of folding: The case of Split Mountain (Utah, USA). *Tectonophysics*, *576–577*, 197–215. https://doi.org/10.1016/j.tecto.2012.07.025

Sayer, Z. R. (1995). *The Nummulitique: Carbonate deposition in a foreland basin setting; Eocene, French alps. (Doctoral dissertation)*. Durham University. Retrieved from http://etheses.dur.ac.uk/6103

Scisciani, V. (2009). Styles of positive inversion tectonics in the Central Apennines and in the Adriatic foreland: Implications for the evolution of the Apennine chain (Italy). *Journal of Structural Geology*, *31*(11), 1276–1294. https://doi.org/10.1016/j.jsg.2009.02.004

Scisciani, V., Calamita, F., Tavarnelli, E., Rusciadelli, G., Ori, G. G., & Paltrinieri, W. (2001). Foreland-dipping normal faults in the inner edges of syn-orogenic basins: A case from the Central Apennines, Italy. *Tectonophysics*, *330*(3–4), 211–224. https://doi.org/10.1016/S0040-1951(00)00229-8

Sepehr, M., Cosgrove, J., & Moieni, M. (2006). The impact of cover rock rheology on the style of folding in the Zagros fold-thrust belt. *Tectonophysics*, *427*(1–4), 265–281. https://doi.org/10.1016/j.tecto.2006.05.021

Silliphant, L. J., Engelder, T., & Gross, M. R. (2002). The state of stress in the limb of the Split Mountain anticline, Utah: Constraints placed by transected joints. *Journal of Structural Geology*, *24*(1), 155–172. https://doi.org/10.1016/S0191-8141(01)00055-4

Sinclair, H. D. (1997). Tectonostratigraphic model for underfilled peripheral foreland basins: An Alpine perspective. *Bulletin of the Geological Society of America*, *109*(3), 324–346. https://doi.org/10.1130/0016-7606(1997)109<0324:tmfupf>2.3.co;2

Smeraglia, L., Mercuri, M., Tavani, S., Pignalosa, A., Kettermann, M., Billi, A., & Carminati, E. (2021). 3D Discrete Fracture Network (DFN) models of damage zone fluid corridors within a reservoir-scale normal fault in carbonates: Multiscale approach using field data and UAV imagery. *Marine and Petroleum Geology*, *126*(December 2020), 104902. https://doi.org/10.1016/j.marpetgeo.2021.104902

Srivastava, D. C. (2000). Geometrical classification of conjugate vein arrays. *Journal of Structural Geology*, *22*(6), 713–722. https://doi.org/10.1016/S0191-8141(00)00005-5

Stearns, D. W. (1968). Certain aspects of fracture in naturally deformed rocks. In R. E. Riecker (Ed.), *NSF advanced science seminar in rock mechanics* (Vol. *1*, pp. 97–116). Air Force Cambridge Research Laboratories.

Stephenson, B. J., Koopman, A., Hillgartner, H., McQuillan, H., Bourne, S., Noad, J. J., & Rawnsley, K. (2007). Structural and stratigraphic controls on fold-related fracturing in the Zagros Mountains, Iran: Implications for reservoir development. *Geological Society, London, Special Publications*, *270*(1), 1–221. https://doi.org/10.1144/GSL.SP.2007.270.01.01

Storti, F., Balsamo, F., Mozafari, M., Koopman, A., Swennen, R., & Taberner, C. (2018). Syn-contractional overprinting between extension and shortening along the Montagna Dei Fiori fault during plio-pleistocene antiformal stacking at the central apennines thrust wedge toe. *Tectonics*, *37*(10), 1–3720. https://doi.org/10.1029/2018TC005072

Storti, F., & Salvini, F. (1996). Progressive rollover fault-propagation folding: A possible kinematic mechanism to generate regional-scale recumbent folds in shallow foreland belts. *AAPG Bulletin*, *80*(2), 174–193. https://doi.org/10.1306/64ED8782-1724-11D7-8645000102C1865D

Storti, F., & Salvini, F. (2001). The evolution of a model trap in the Central Apennines, Italy: Fracture patterns, fault reactivation and development of cataclastic rocks in carbonates at the narni anticline. *Journal of Petroleum Geology*, *24*(2), 171–190. https://doi.org/10.1111/j.1747-5457.2001.tb00666.x

Tavani, S., Mencos, J., Bausà, J., & Muñoz, J. A. (2011a). The fracture pattern of the Sant Corneli Bóixols oblique inversion anticline (Spanish Pyrenees). *Journal of Structural Geology*, *33*(11), 1662–1680. https://doi.org/10.1016/j.jsg.2011.08.007

Tavani, S., Storti, F., Fernández, O., Muñoz, J. A., & Salvini, F. (2006). 3-D deformation pattern analysis and evolution of the Añisclo anticline, southern Pyrenees. *Journal of Structural Geology*, *28*(4), 695–712. https://doi.org/10.1016/j.jsg.2006.01.009

Tavani, S., Storti, F., Lacombe, O., Corradetti, A., Muñoz, J. A., & Mazzoli, S. (2015a). A review of deformation pattern templates in foreland basin systems and fold-and-thrust belts: Implications for the state of stress in the frontal regions of thrust wedges. *Earth-Science Reviews*, *141*, 82–104. https://doi.org/10.1016/j.earscirev.2014.11.013

Tavani, S., Storti, F., Salvini, F., & Toscano, C. (2008). Stratigraphic versus structural control on the deformation pattern associated with the evolution of the Mt. Catria anticline, Italy. *Journal of Structural Geology*, *30*(5), 664–681. https://doi.org/10.1016/j.jsg.2008.01.011

Tavani, S., Storti, F., Soleimany, B., Fallah, M., Muñoz, J. A., & Gambini, R. (2011b). Geometry, kinematics and fracture pattern of the Bangestan anticline, Zagros, SW Iran. *Geological Magazine*, *148*(5–6), 964–979. https://doi.org/10.1017/S0016756811000197

Tavani, S., Vignaroli, G., & Parente, M. (2015b). Transverse versus longitudinal extension in the foredeep-peripheral bulge system: Role of Cretaceous structural inheritances during early Miocene extensional faulting in inner central Apennines belt. *Tectonics*, *34*(7), 1412–1430. https://doi.org/10.1002/2015TC003836

Van Geet, M., Swennen, R., Durmishi, C., Roure, F., & Muchez, P. H. (2002). Paragenesis of Cretaceous to Eocene carbonate reservoirs in the Ionian fold and thrust belt (Albania): Relation between tectonism and fluid flow. *Sedimentology*, *49*(4), 697–718. https://doi.org/10.1046/j.1365-3091.2002.00476.x

Veizer, J., Ala, D., Azmy, K., Bruckschen, P., Buhl, D., Bruhn, F., et al. (1999). 87Sr/86Sr, δ13C and δ18O evolution of Phanerozoic seawater. *Chemical Geology*, *161*(1), 59–88. https://doi.org/10.1016/S0009-2541(99)00081-9

Vilasi, N., Malandain, J., Barrier, L., Callot, J. P., Amrouch, K., Guilhaumou, N., et al. (2009). From outcrop and petrographic studies to basin-scale fluid flow modelling: The use of the Albanian natural laboratory for carbonate reservoir characterisation. *Tectonophysics*, *474*(1–2), 367–392. https://doi.org/10.1016/j.tecto.2009.01.033

Villars, F. (1986). Structure et cinematique des deformations dans la chaine des Aravis (Zone delphino-helvetique, Haute-Savoie, France): Implications regionales. *Geologie Alpine*, *62*, 107–116.

Vitale, S., Dati, F., Mazzoli, S., Ciarcia, S., Guerriero, V., & Iannace, A. (2012). Modes and timing of fracture network development in poly-deformed carbonate reservoir analogues, Mt. Chianello, southern Italy. *Journal of Structural Geology*, *37*(15), 223–235. https://doi.org/10.1016/j.jsg.2012.01.005

Welbon, A. I. (1988). The influence of intrabasinal faults on the development of a linked thrust system. *Geologische Rundschau*, *77*(1), 11–24. https://doi.org/10.1007/BF01848673

Welbon, A. I., & Butler, R. W. H. (1992). Structural styles in thrust belts developed through rift basins: A view from the western Alps. In R. M. Larsen, H. Brekke, B. T. Larsen, & E. Talleraas (Eds.), *Structural and tectonic modelling and its application to petroleum geology, NPF special publication* (Vol. *1*, pp. 469–479). Elsevier. https://doi.org/10.1016/B978-0-444-88607-1.50037-1

Wildi, W., & Huggenberger, P. (1993). Reconstitution de la plate-forme européenne anté-orogénique de la Bresse aux Chaînes subapines; éléments de cinématique alpine (France et Suisse occidentale). *Eclogae Geologicae Helvetiae*, *86*(1), 47–64.